POLITECNICO DI MILANO

Scuola di Ingegneria dei Sistemi

Corso di Laurea Magistrale in Ingegneria Fisica

Dipartimento di Fisica

ATOMIC SCALE INVESTIGATION OF THE EARLY STAGES OF COBALT OXIDATION

Relatore: Prof. Lamberto DUÒ

Correlatore: Prof. Alberto BRAMBILLA

Candidato:
Oleh IVASHKO
Matr. 801364

Anno Accademico 2013 - 2014

Contents

List of Figures

Abstract

In this thesis work early stages of oxidation of a ultra-thin film of metastable cubic cobalt was studied. The film was deposited, with the Molecular Beam Epitaxy (MBE) technique, on a Fe(001)-$p(1x1)$O substrate. The subsequent oxidation (from 2 L up to 500 L) was performed with the post oxidation technique heating the film at 200°C.

To study the above sample Auger Electron Spectroscopy (AES), Low Energy Electron Diffraction (LEED) and Scanning Tunneling Microscopy (STM) were used.

The crystalline structure of the iron substrate and the cobalt film was investigated by LEED. From the AES data, it was possible to observe that oxygen floats to the surface during the cobalt deposition and that there is low intermixing of iron with the uppermost film. Moreover, it was observed that the oxidation takes place only on the surface of the cobalt film. A small oxidation of the iron substrate was anyway not excluded.

From the STM data, it was possible to distinguish metallic cobalt from oxide islands, which present a relative height variation with respect to the different tunneling parameters. The coverage analysis of the first and the second oxide layers confirm a layer-by-layer growth mode.

A topographic study evidences the presence of states in the oxide gap, whose nature is attributed to surface defects and to the coupling at the interface with the metallic cobalt. An electronic gap of 2.3 eV was estimated by Scanning Tunnelling Spectroscopy (STS) measurements. It was also detected a band bending in the oxide, attributed to a charge transfer at the surface and/or at the interface with the underlying cobalt.

Supported by the topographic study, CoO was seen to grow in the rocksalt structure rotated in plane by 45°, with respect to the bct cobalt lattice, exposing the CoO(001) surface.

Abstract

In questo lavoro di tesi sono state studiate le prime fasi di ossidazione di un film ultrasottile di cobalto metastabile. Il film di cobalto è stato depositato, con la tecnica Molecular Beam Epitaxy (MBE), sul substrato Fe (001)-*p*(1x1)O. La successiva ossidazione (da 2 L fino a 500 L) è stata eseguita con la tecnica di post-ossidazione riscaldando il campione a 200°C.

Per studiare il suddetto campione sono state utilizzate Auger Electron Spectroscopy (AES), Low Energy Electron Diffraction (LEED) e Scanning Tunneling Microscopy (STM).

Una struttura cristallina del substrato di ferro e del film di cobalto è stata indagata con il LEED. Dai dati AES, è stato possibile osservare che l'ossigeno segrega sulla superficie durante la deposizione di cobalto e che si verifica un ridotto intermixing di ferro con il film soprastante. Inoltre, è stato osservato che l'ossidazione avviene solo alla superficie di cobalto. Comunque, una ridotta ossidazione del substrato di ferro non è stata esclusa.

Dai dati STM, è stato possibile distinguere il cobalto metallico dalle isole di ossido, che presentano una variazione di altezza (misurata dal substrato di cobalto) cambiando i parametri di tunneling. Un'analisi di coverage (ricoprimento) del primo e del secondo strato di ossido, confermano una modalità di crescita layer-by-layer.

L'analisi topografica evidenzia la presenza di stati nella gap dell'ossido, i quali sono stati attribuiti alla presenza di difetti superficiali e all'accoppiamento all'interfaccia dell'ossido con il cobalto metallico. Una gap di 2.3 eV è stata stimata con le misure STS (Scanning Tunneling Spectroscopy). È stato inoltre rilevato un band bending dell'ossido, attribuito ad un trasferimento di carica in corrispondenza della superficie e/o all'interfaccia con il cobalto sottostante.

Sulla base dei risultati topografici, CoO è stato visto crescere con la struttura rocksalt ruotata di 45° rispetto al reticolo bct del cobalto, esponendo la faccia CoO(001) alla superficie.

Sintesi

In questo lavoro di tesi sono stati studiati i primi stadi di ossidazione di un film ultrasottile di cobalto metastabile depositato su un substrato di ferro (Fe(001)-p(1x1)O). La tecnica usata per la deposizione è Molecular Beam Epitaxy (MBE). L'ossidazione è stata svolta esponendo il campione (riscaldato a 200°C) all'ossigeno molecolare. L'esposizione all'ossigeno viene misurata in langmuir (L). Il campione è stato esposto progressivamente a partire da 2 L fino ad arrivare a 500 L.

La preparazione del campione e il successivo studio sono state svolte in condizioni di ultra-alto-vuoto (UHV), ad una pressione di circa $p \sim 7 \cdot 10^{-11}$mbar. Tali condizioni sono necessarie principalmente per due ragioni: durante la preparazione del campione si vuole diminuire al minimo la quantità di gas residui che potrebbero contaminare il campione; inoltre siccome il libero cammino medio degli elettroni è molto piccolo a pressione ambiente, si ha la necessità di avere pressioni estremamente basse per poter utilizzare le tecniche investigative. Per maggiori informazioni si rimanda al Capitolo 1.

Le tecniche investigative utilizzate in laboratorio sono Low Energy Electron Diffraction (LEED), Auger Electron Spectroscopy (AES) e Scanning Tunneling Microscopy (STM). Il LEED si basa sul fenomeno di diffrazione degli elettroni incidenti su un reticolo regolare, perciò viene utilizzato per verificare la cristallinità del campione e le possibili ricostruzioni superficiali. L'AES si basa sul fenomeno Auger: gli elettroni incidenti creano una lacuna di core, un elettrone ad un livello energetico superiore decade in modo non radiattivo trasferendo l'energia ad un'altro elettrone (elettrone Auger). Analizzando l'energia cinetica di quest'ultimo si può risalire alle transizioni accadute durante il processo. Siccome ogni elemento presenta un ben specifico spettro energetico, AES è utilizzato per studiare la composizione chimica del campione. L'STM, invece, si basa sull'effeto tunnel (effetto puramente quantistico): un elettrone ha una probabilità non nulla di attraversare un barriera di potenziale, fisicamente impossibile in meccanica classica. L'implementazione strumentale di tale effetto consiste in una sottile punta di tungsteno che viene avvicinata al campione in questione. La punta

viene prodotta tramite l'erosione chimica (etching) adoperando NaOH come elettrolita. Mentre il campione resta fermo il movimento della punta viene prodotto da dei piezoelettrici che permettono un controllo del movimento dell'ordine dell'angstrom (Å). Applicando una determinata tensione al campione (punta a massa), risulta una corrente elettrica (corrente di tunneling). Durante una scansione, acquisendo la corrente in ogni punto viene ricostruita un'immagine topografica del campione. Per maggiori dettagli sulle tecniche investigative si rimanda al Capitolo 2.

L'ultima parte della tesi riguarda la presentazione e la discussione dei dati sperimentali (Capitolo 3). In breve, il modo di crescita dell'ossido di cobalto per i primi due layer è stato verificato di essere layer-by-layer. I dati AES confermano che l'ossidazione riguarda solo il film sottile di cobalto e non interessa il substrato di ferro sottostante. Si è confermata l'effettivo sviluppo dell'ossido grazie ai dati STM, i quali presentano un variazione relativa dell'altezza delle isole di ossido (rispetto al substrato metallico di cobalto) cambiando i parametri di tunneling (corrente e specialmente la tensione applicata). Questo effetto è dovuto alla presenza della gap elettronica tra le bande di valenza e di conduzione. Sono inoltre stati osservati stati nella gap probabilmente dovuti alla presenza di difetti superficiali (mancanze di ossigeno) e/o dall'accoppiamento all'interfaccia dell'ossido con il metallo sottostante.

Grazie ai dati STS (Scanning Tunneling Spectroscopy) un gap di 2.3 eV è stata misurata. Inoltre si è osservato uno spostamento del livello di Fermi dell'ossido di 0.35 eV verso la banda di conduzione. Questo fenomeno è dovuto ad un trasferimento di carica dovuto ai difetti superficiali (mancanza di ossigeno) e/o alla barriera di Schottky che si crea all'interfaccia con il cobalto. È stato ipotizzato un modello di crescita della struttura rocksalt di CoO sul cobalto metastabile bct. Da questo modello risulta una rotazione nel piano di 45° della cella di CoO rispetto alla cella bct. Da cui risulta che la faccia CoO(001) è esposta alla superficie.

Introduction

The initial stages of metal oxidation have been of particular interest in applied and fundamental research for several decades. Indeed, almost every metal surface exposed to oxygen-rich environment is covered by a thin native oxide film. This oxide skin covering the metal is of fundamental importance as a protection against corrosion [1, 2].

Their importance is also backed by the peculiar properties they posses such as, for instance, high electrical resistivity, mechanical hardness, excellent temperature stability and chemical inertness.

For these reasons oxide materials find a widespread application in many technological fields.

One important example is in the field of the heterogeneous catalysis, where they are used to stabilize small metal particles which acts as chemically-active species [3]. Moreover, under particular circumstances, oxides can play an important role also as active substrates, thanks to their ability to release and store oxygen [4], exchange charges with the active components [5, 6], etc.

Furthermore oxides became important in micro-electronics after the invention of field-effect transistor [7]. Because of the effort to minimize the electronic devices size, research is ongoing to find materials with better dielectric properties and spatial self-organized homogeneity [8]. Again, oxides can be used in solar cells[9], super-conducting elements [10] and chemical sensors [11]. For antiferromagnetic transitional oxides further implementation can be found in digital data-storage devices and spintronics [12].

This thesis work deals with the early stages of oxidation of ultra-thin cobalt films grown on Fe(001). A short overview of oxides with more effort on CoO will be exposed in this chapter. The description of the experimental setup will be discussed in Chapter 1 and Chapter 2. In Chapter 3 the experimental data will be presented an discussed.

Metal Oxides

Along with a renowned technological importance, oxides present a large variety of chemical and physical properties that motivates research in fundamental science. While binary bulk metal oxides properties are almost completely understood [13, 14], the same is not true for what regards the surfaces. In comparison to the metal and semiconductor samples, oxides exhibits a large variety of modifications from bulk-like crystals which strongly affects the electronic and magnetic states, as well as optical and conduction properties. The reason can be attributed to the high degree of bond saturation and chemical inertness.

One of the main complexity encountered is the surface reconstruction of bulk-like unit cell. Only in few cases surface termination is close to the unperturbed bulk lattice, while more often, atoms position rearrangement takes place. To study the surface reconstruction one can cut a bulk crystal through one particular lattice direction or may grow a thick film on a specific metal substrate (which is common in STM analysis, see p.19) with desired surface symmetry. As a consequence the resultant surface stoichiometry and ordering depends on the substrate interaction and on the particular direction in comparison to the bulk lattice (which determines the direction and number of the dangling bonds). The equilibrium structure of the surface is obtained minimizing the Gibbs free-energy [15], but also the environment can influence the surface formation, e.g. oxygen partial pressure and residual gases [16, 17]. Thus the surface evolution, in the surrounding gas phase, can be kinetically hindered to the lowest-energy configuration forming a metastable compound.

Depending on the unit cell of bulk crystal and on the direction exposed, surface can be terminated with either oxygen or metal layer [18, 19] or with a stoichiometric mixing of both. For ionic oxides such a distinction play an important role in reconstructions, which originate from a delicate equilibrium of cations and anions in bulk crystal [20]. For surfaces with equal distribution of metal and oxygen atoms, e.g. rocksalt(001) planes, only a small buckling (regular displacement of ions from bulk-like structure) is observed. For systems where metal and oxide ion planes are alternated, instead, reconstructions and thermodynamic instabilities (diverging of electrostatic energy) occurs. This is the case of rocksalt(111) planes, e.g. MgO(111) and NiO(111) [21], which are also unaffected by reconstructions (that may decrease the electrostatic energy) due to the rigid crystal structure.

Another important aspect of oxides is the absence of free electrons. Structural defects, thus, are hardly screened and, as a consequence, the electronic and chemical properties are altered in respect to the perfect crystal [22, 23]. Some examples of near-surface defects are point defects, step edges, intersti-

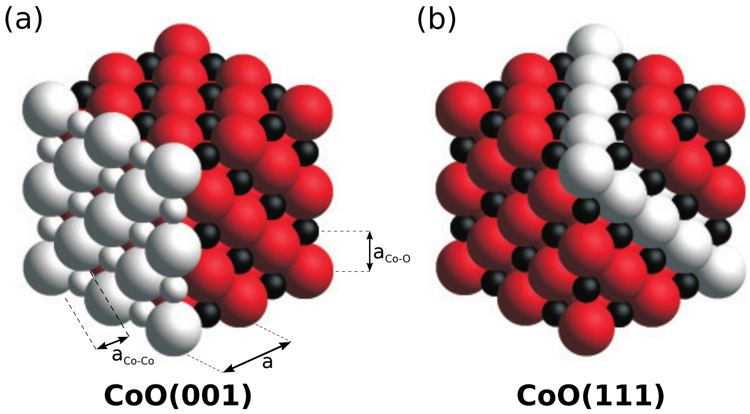

Figure 1: Schematic representation of CoO rocksalt structure. Cobalt and oxygen atoms are respectively red and black balls, while the white enhance the visualization of (001) (a) and (111) (b) lattice planes. In figure (a) are also shown the characteristic parameters: lattice constant a=4.267 Å, cobalt-cobalt distance a_{Co-Co}=3.017 Å and cobalt-oxygen distance a_{Co-O}=2.133 Å [29].

tial atoms and kink and corner sites. For oxides, the most relevant are the oxygen vacancies, which are also termed color or F centers due to their effect on optical properties [24]. The main effect of these defects is the perturbation of the local electronic structure, introducing for instance discrete states in the gap (like a dopant) and additional deformations of the surface.

Cobalt Oxide: State Of The Art

Bulk cobalt oxide (CoO phase) is one of the most studied Mott insulators. Conventional band theory predicts metallic behaviour [25] of CoO, while experimental result evidence the presence of band gap [26]. Peierls and Mott [27] pointed out that band theory may fail when the intersite tunnelling of electrons is suppressed by the Coulomb on-site repulsion between electrons. Nevertheless the calculation of the electronic states still remains an open problem. On the other hand x-ray photoelectron spectra [28] revealed that CoO is a charge-transfer insulator where the band gap separates filled oxygen $2p$ and empty metal $3d$ bands.

Cobalt monoxide has a rocksalt structure (Fig.1) with a lattice constant of $a = 4.267$ Å. The minimum distance between two cobalt (or oxygen) atoms is $a_{Co-Co} = 3.017$ Å, which also corresponds to one monolayer (ML) if the crystal is prepared exposing the (111) surface. The distance from one cobalt to one oxygen atom is $a_{Co-O} = 2.133$ Å, which is the height of 1 ML along the [001] direction.

Even if the electronic structure of CoO could not be calculated, the accurately band gap size can be experimentally obtained. Powell and Spicer [30], using optical reflectance spectra, obtained a gap of 5.5 eV. While van Elp et.al. [31] using x-ray photoemission spectroscopy (XPS), bremsstrahlung isochromat spectroscopy (BIS) and x-ray-absorption spectroscopy observed a gap of 2.5 eV. To explain this discrepancy van Elp observed that Powell and Spicer, confronting CoO with NiO optical data, set the cobalt oxide edge when a strong rise of adsorption spectrum is occurred, which is larger than that of nickel oxide (4 eV). However, the shape of the edge is quite different in these two materials. In fact the onset is more broader in CoO than in NiO. As a result a smaller gap size is expected with a weaker optical adsorption, as was confirmed with the data of Pratt and Coelho [32], where the adsorption onset occurs between 2.5 and 3.0 eV.

Another stable cobalt oxide phase is Co_3O_4, which presents a spinel structure with Co^{2+} on the tetrahedral and Co^{3+} on the octahedral sites of the lattice. Contrary to the CoO phase, its electronic structure is well known and the gap is found to be 1.6 eV [31].

Apart from single crystals, CoO has been reported to epitaxially grow on metallic substrates. On Ag(001) various coverages at different temperatures has been investigated. At room temperature 1.2 ML (nominal in the [001] direction) grow with a high roughness but with a successive annealing, up to 390 K, large flat islands are observed [33]. For a high substrate temperature ($440 - 470$ K) a layer-by-layer growth mode is observed up to 10 ML [34]. It was clearly visible that this thickness is sufficient to study CoO bulk-like electronic structure since the substrate contribution (from the interface) is suppressed. With another experiment, at the same temperature, it was observed that in-plane cobalt oxide lattice parameter is in registry with the silver substrate up to 4 ML (the mismatch, Eq.1.2, is about 4%) [35]. Topographic study of 5 ML of CoO exhibits a gap of 2.2 eV [36] which is in agreement with the bulk one. At higher temperature (670 K), for coverages above 3 ML of CoO a relaxation process can be detected [8]. In fact in-plane lattice parameter start to change and at 8ML a dislocation network, at interface with Ag, is observed. When reaching 23 ML of CoO, hte measured lattice parameter (2.98 Å) is close to the bulk one (3.02 Å) and a dislocation network is fully evolved with a periodicity that can be interpreted in terms of coincidence-lattice model.

Another substrate frequently used is Ir(001) in its metastable (1x1) structure. Up to 4 ML CoO(111) polar structure grows epitaxially at 520K but when the substrate is precovered with oxygen, also the Co_3O_4 phase in submonoleyer range is observed [37]. Due to the high mismatch of CoO(111), with respect to the substrate, a distorted quasi-hexagonal structure is obtained in a c(10x2) superstructure whitin first few monolayers [38]. For higher thickness films ($20 - 40\,\text{Å}$), annealed at high temperatures ($670 - 770\,\text{K}$), a hexagonally-like LEED (see p.16) pattern is observed [39]. Both cobalt oxide phases (111) structures are thus consistent whit respect to the symmetry, but with spot-distance analysis Co_3O_4 is unequivocally recognized. CoO(001) is not observed in neither coverage despite the cubic symmetry of the (1x1) structure.

On Pd(100) substrates, a coverage dependent evolution is observed [40]. For low coverage regimes (up to $2 - 3\,\text{ML}$), the CoO phase is detected with (100) and (111) terminations. For higher coverages ($10 - 20\,\text{ML}$) both CoO(100) and $Co_3O_4(111)$ phases heve been observed in ratios dependent on the preparation conditions.

Also on Pt(111) substrates, the evolution of cobalt oxide layer has been investigated [41]. Oxidizing 1 ML of Co at room temperature and at 470 K produces a rough surface, while at higher temperature ($570 - 740\,\text{K}$) a perfect moiré pattern is observed. In this latter case a CoO(111) bilayer is detected whit a slight distortion from the bulk-like symmetry. Also an insufficient oxidation was performed on 1 ML resulting in a triangular moiré (3x3) structure. For such low coverages the band gap has not been observed. For a higher cobalt oxide thickness a Stransky-Krastanov mode is observed. The 3D growth mode seems to be unaffected to the temperature and the CoO(111) bulk-like structure is observed.

Cobalt oxide was also studied on other substrates but even with these few examples it is clear that, like for every other oxide, the evolution and orientation of CoO and/or Co_3O_4 depends principally by the underlying lattice parameters and symmetry, temperature and the oxygen environment.

Also the magnetic properties of cobalt oxide are still an important argument of technological and fundamental research. Like for other transition metal oxides, CoO is antiferromagnetic (Neél temperature of about 292 K) but the strength of this magnetic ordering is dependent on the substrate, i.e. on the strain force resulting from lattice deformation from the bulk structure [42]. Using a ferromagnetic substrate or incorporating a thin cobalt oxide in spin valve structures a magnetic coupling is thus established. However this arguments are out of current thesis. For more details on CoO magnetic properties see [12, 43].

Chapter 1

Sample Preparation

In order to create well structured thin films, with minimum grade of contamination, the main request is to operate in Ultra-High Vacuum (UHV) condition which means have the pressure $p < 1 \cdot 10^{-9}$mbar . For this purpose our samples are prepared and studied at a pressure of about $7 \cdot 10^{-11}$mbar. The experimental apparatus used, shown in Fig. 1.1, is composed of two interconnected chambers. In the first (prep-chamber) it is possible to prepare the sample and to study its chemical composition and structural ordering. In the second (STM-chamber) instead there is a Scanning Tunnelling Microscope (STM), which gives structural superficial ordering in real space and also the information of density of states with Scanning Tunnelling Spectroscopy (STS). The preparation of the sample is done by Molecular Beam Epitaxy (MBE), while its study by Low Energy Electron Diffraction (LEED) and Auger Electron Spectroscopy (AES). The purpose of this chapter is to describe how the UHV conditions is reached and maintained, and how the sample is prepared, while the investigation techniques are described in Chapter 2.

1.1 Pumping System

In order to reach UHV conditions several pumping systems are used: one turbomolecular pump baked by one rotary-vane pump, two titanium sublimation pumps (TSP) and two sputter-ion pumps.

The rotary-vane pump is used to reach 10^{-2}mbar that permits the turbomolecular pump to operate in its working regime. This pump is the simplest one and consists of an eccentric rotator that expands the gas in inlet and compresses it in outlet. The upper limit of the rotary-vane pump is about 10^{-4}mbar.

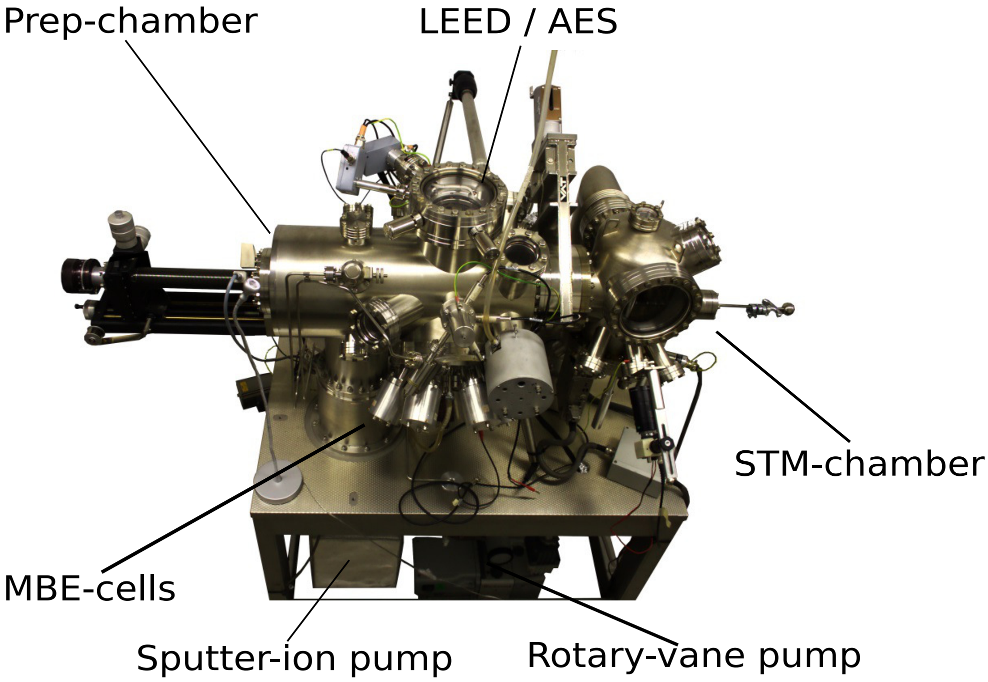

Figure 1.1: Experimental apparatus made of stainless-steel: prep-camber contain MBE-cells (growing) and LEED/AES (investigation); while STM-chamber contain STM. The two chamber are separated by the gate valve. There are also shown two of the four used pumps to reach UHV condition.

Also the turbomolecular pump consists of a rotary part but it's made in a way that permits to reach and maintain the UHV conditions. This pump (Fig.1.2(a)) presents many lamellae inclined to an angle that maximize the probability to move the molecules towards the exhaust. The lamellae are connected to a rotary central part that works at 15 000 - 30 000 rpm. Both the turbomolecular pump and the rotary-vane pump, are sources vibrations. Such vibrations can disturb the STM imaging and so the pumps are turned off during the measurements. To maintain the UHV conditions, hence, the sputter-ion pumps and TSP, the so called sorption pumps, are used, that also allow to obtain pressures below 10^{-11}mbar.

Sputter-ion pumps (Fig. 1.2(b)) consist of a few cylindrical stainless-steel anodes, two Ti plates (cathodes) and a magnet that generates a magnetic field along the anode axis. The magnetic field allows to increase the probability, of the electrons, emitted from the cathode, to hit the residual gases in the helical trajectories. The voltage applied to the anode is about 3 - 7 kV, so the emitted electrons possess a high kinetic energy. The result of the collisions between electrons and molecules are positive ions that are accelerated to the

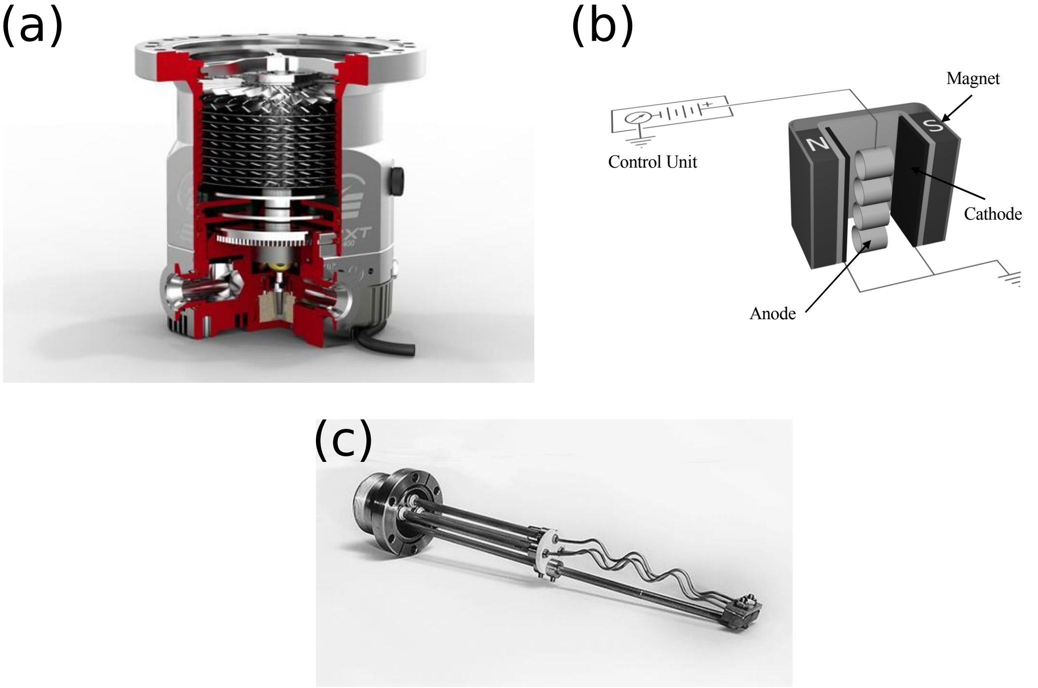

Figure 1.2: (a) Turbomolecular pump; (b) Sputter-ion pump; (c) Titanium Sublimation Pump (TSP)

cathode. When the ions reach the Ti-cathode they can be chemisorbed or physisorbed. In some cases they also can penetrate a few atomic layers and, consequently, be buried. With this mechanisms the residual gases like H_2, O_2, CO, CO_2, N_2 and H_2O can be drastically reduced and consequently the pressure decreases.

The TSP consists of a titanium-molybdenum alloy wire (in Fig.1.2(c)) there are three filaments for interchanging) through which passes a current of 40 - 50 A. This high current sublimates instantly the superficial Ti that diffuses within the chamber and attaches to the walls forming a layer of clean Ti. When a molecule hits this layer it reacts with Ti and forms a stable component that remain sticked to the walls. So the pressure in the chamber is reduced. After some period of time (that depends of the pressure inside the chamber) the layer of Ti became not enough clean and the TSP should be turned on again. Typically it's turned on automatically according to the trend of the pressure. It should be noted that TSP works well with more reactive molecules (e.g. CO and O_2) and in generally it doesn't work with inert molecules (e.g He_2).

Although the efficiency of the described pumps pressures under 10^{-8}mbar are reached in a long time. In fact when the system is open to air, the walls of the chamber are covered with a layer of water. During the pumping process this water desorb with a very low rates. As a consequence the pressure decreases slowly. To avoid this problem a so-called *bake-out* is performed. The chamber is heated at about 170°C. This causes high desorption of H_2O molecules and initially the pressure increases even up to 10^{-6}mbar. When the pressure reaches 10^{-8}mbar, typically after 48 hours, the system is brought back to room temperature. This simple process permits to pump away the large part of the water and the system attain the UHV conditions in a reasonable time.

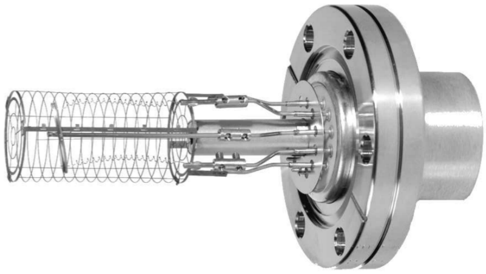

Figure 1.3: Bayard-Alpert ion-gauge.

The discussion above regards the achievement of UHV conditions but a few words might be spent about the instruments measuring such low pressure, i.e. vacuum gauges. In laboratory we use two (one for each chamber) Bayard-Alpert ion-gauges (Fig. 1.3) for a pressure measurement in the range from 10^{-4}mbar and 10^{-11}mbar. This vacuum gauge consists of a cylindrically grid (anode) around the hot W filament (cathode) and a wire (collector). The electrons are emitted from the cathode and accelerated to the anode acquiring a high kinetic energy. The residual gases are consequently ionized and attracted by the collector producing an electric current. The acquired current is then processed and converted into a pressure.

Note that a vacuum gauge is needed not only to verify the pressure achieved but also to monitor the sample preparation, e.g. growing and oxidation (in the present work a typical partial pressure of 10^{-8}mbar of O_2 molecules is employed).

1.2 Sample Preparation

In order to prepare higher ordered and contaminants free films, the UHV conditions, described above, are required, which in addition permits to investigate the sample for a relative long time ($\sim 1\,\text{day}$). Nevertheless preparation techniques are required as every sample (film or substrate) has been exposed to atmospheric pressure before entering in UHV chamber.

1.2.1 Sample Cleaning

Cleaning techniques are usually adopted to prepare the substrate on which a desired film is to be grown. Consecutive cycles of *sputtering* (noble gas ion-bombardment) and *annealing* (heating) are performed for this purpose.

Sputtering is used to remove the first few layers that are covered by contaminants. In our case, an Ar gas flux, regulated by a *leak-valve*, is ionized by electrons produced by thermionic effect from a W wire. A permanent magnet is used in order to increase the efficiency of the above mechanism. The Ar^+ ions are then accelerated with high voltage ($\sim 1.5\,\text{kV}$) while the sample is connected to ground trough an amperometer. Sputtering rate is monitored measuring the current on the sample ($\sim 10\,\mu\text{A}$). The collision between ions and the sample generates a linear collision cascade process. Energy is transferred from Ar^+ ions to the sample. If the kinetic energy is large enough, the sample atoms can escape from the surface with an efficiency that is directly proportional to the ratio between target and beam mass.

Once the sputtering is complete, the surface of the sample presents a low crystallographic ordering and high roughness. Annealing process is thus performed in order to recreate an ordered surface. Thermal energy allows the surface atoms to diffuse and reach energy favourable sites. As a consequence, large flat terraces are formed. In addition this heating process allows contaminants diffusion to the surface and their partial desorption. By iterating a few cycles of sputtering and annealing a clean and high-ordered surface is obtained.

1.2.2 Films Growth

In order to grow a thin film the technique adopted in laboratory is Molecular Beam Epitaxy (MBE). In the evaporation cell there is a high purity cylindrical shape material (rod) around which is wrapped a W wire. A current of about $4-5\,\text{A}$ produces electrons which impacts on the rod at a high voltage ($\sim 2.5\,\text{kV}$). As a result, a regular flux of atoms is produced by a superficial sublimation. The MBE technique is typically feasible for metals as the sublimation temperature is less than that of fusion.

It is important to note that the flux of atoms is exponentially proportional to the total electric power dissipated in the material. Thus the growth rate is controlled with power via a feedback loop.

In order to calibrate a desired flux (varying the power) a quartz thickness monitor, which employs piezoelectric resonance of the single quartz crystal, is used. The resonance frequency is proportional to the total mass of the crystal, approximately as $f \sim m^{-1/2}$. Due to a condensation of the atoms on the crystal (which thus change gradually its mass) it is possible to extract the flux value. Thanks to the accurate calibration the deposition rate can be controlled down to some fractions of single atomic layer, or monolayer (ML), per minute.

Sublimated atoms, before impinging on the sample surface forming the condensate phase, are in their gaseous phase. When they reach the surface an instantaneous re-evaporation or diffusion may occur. In the latter case the particle might lead to adsorption, mainly on step edges or other kind of defects, or again it may re-evaporate. Principally a balance between the gaseous phase and the condensed one is obtained during a film growth.

Three main film growth modes can be distinguished (Fig.1.4). If the interaction between substrate and layer atoms is stronger than the interaction between neighbouring atoms, a *layer-by-layer* (Frank-van der Merve) growth mode occurs, which corresponds to a perfect wetting of the substrate and a high quality film is obtained. The subsequent layer starts to grow only when the latter is complete. When the interaction with the substrate is much lower than that with film atoms, *island* (Vollmer-Weber) growth mode takes place. In this case different atomic layers are exposed producing a high rugosity film surface. The intermediate case is *layer-plus-island* (Stransky-Krastanov) growth mode. After the completion of one layer, island formation occurs.

The reasons of this different growth modes can be partially explained in terms of surface tensile energy γ and mismatch f between bulk cell parameters. In the former case three main energies should be considered, i.e. surface free energy of interaction between substrate and vacuum (γ_{SV}), film and vacuum (γ_{FV}) and film and substrate (γ_{FS}). The resultant equilibrium equation is

$$\gamma_{SV} = \gamma_{FS} + \gamma_{FV} \cos\phi, \tag{1.1}$$

where ϕ is the contact angle between substrate and film. For the perfect wetting, i.e. Frank-van der Merve growth mode, the requirement is $\phi = 0$ which corresponds to $\gamma_{SV} \geqslant \gamma_{FS} + \gamma_{FV}$. In the case of Vollmer-Weber growth mode $\phi > 0$ and we obtain $\gamma_{SV} < \gamma_{FS} + \gamma_{FV}$.

On the contrary Stransky-Krastanov growth mode can be explained con-

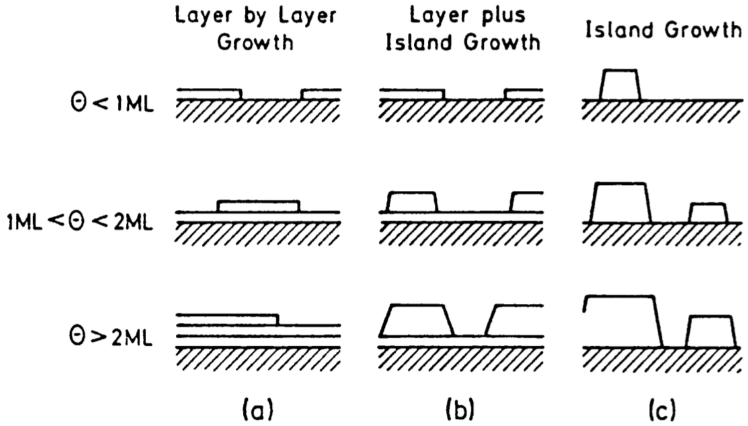

Figure 1.4: Schematic representation of film growth for different coverage (Θ) regimes. (a) Layer-by-layer growth (Frank-van der Merve). (b) Layer-plus island growth (Stranski-Krastanov). (c) Island growth (Vollmer-Weber) [44].

sidering the mismatch

$$f = \frac{a_f - a_s}{a_s}, \tag{1.2}$$

where a_s and a_f are the (cubic) lattice parameters of the substrate and film respectively. For large mismatch values, strain forces propagates along the film. In fact, in the first few MLs, the film tries to adjust its lattice parameter to the substrate one, and if this strain exceeds the interaction energy between adjacent atoms, island formation occurs. Stransky-Krastanov growth mode takes place when the grown material prefers to organize in its bulk-like crystal unit cell. Indeed when the film tend to follow the symmetry and lattice parameter of the surface 2D unit cell it is common to talk about *epitaxy*. A typical accepted value for epitaxial growth is $f < 0.04$.

Once a suitable substrate or thin film is prepared, the oxide growth can be performed. To prepare a thin film of an oxide, a certain quantity of oxygen (tipically O_2 molecules) must be introduced into the vacuum chamber. To control a the oxigen exposure, a *leak-valve* is used in our laboratory. The exposure of oxygen is measured in Langmuir[1] (L). If one assume that when every molecule impinging on the surface sticks on it, 1 L corresponds approximately to 1 ML of oxygen. Even if the sticking coefficient[2] of oxygen

---

[1] $1\text{L}=10^{-6}\text{Torr s}=1{,}33\cdot10^{-6}\text{mbar s}$.

[2] Sticking coefficient is defined as the ratio between adsorbed particles and the total number of atoms/molecules impinging on the surface. Therefore the maximum value is 1 (all particles adsorbs), while the minimum is 0 (neither particle is adsorbed).

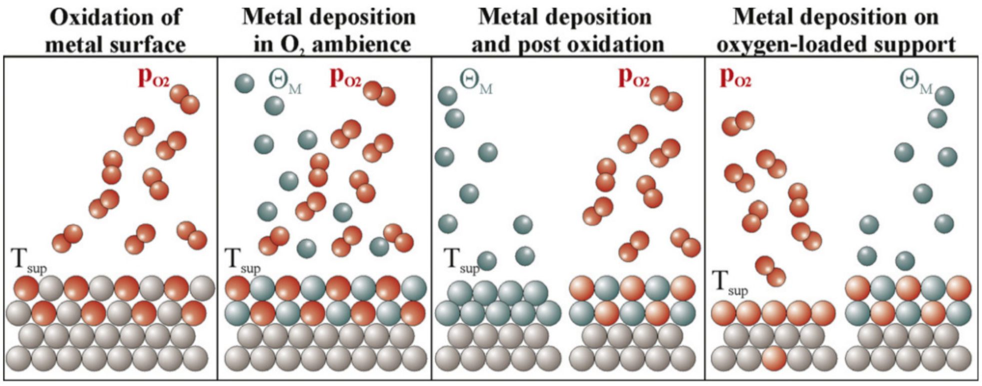

Figure 1.5: Sketch of different oxide film growth [45]. Important parameter during the oxide preparation are temperature T_{sup} of the support (substrate or thin film), partial pressure p_{O_2} of oxygen and the deposition rate Θ_M of the metal.

is generally close to 1 (which is the maximum value) a higher quantity of oxygen is usually used. The eventual abundance of oxygen can be removed by heating the sample.

There are a few procedures used to growth an oxide, which are schematically represented in Fig. 1.5. Direct oxidation (oxygen exposure) can be performed on a suitable high ordered metal substrate (Fig. 1.5). Oxygen, by diffusing under the surface, reaches a more energetically favoured positions creating a well ordered oxide crystal. An important aspect is that oxidation of the first few monolayers act as a passivating layer. As a consequence, a further oxide growth is inhibited and a higher oxygen exposure must be performed to increase the oxide thickness. Another procedure is the *reactive deposition* (2^{nd} panel of Fig. 1.5). In this case metal film is grown in oxygen saturated atmosphere. As a consequence, arbitrary oxide film thicknesses can be reached since passivation is absent. The last approach to grow an oxide is the *post-oxidation* at high temperature. It is similar to the first described method but the difference is that a thin film is grown onto the substrate to obtain a certain surface orientation which is not possible in bulk crystals for the particular material. In this case a high temperature is required to enhance the interlayer diffusion in order to obtain a high ordered and arbitrary thick oxides.

In some cases, before the oxide preparation the sample can be covered with a layer of oxygen (last panel of Fig. 1.5). The O-rich precursor state increase the availability of oxygen during the film growth.

Chapter 2

Sample Investigation

Once the sample is prepared the chemical and structural properties can be investigated using Auger Electron Spectroscopy (AES), Low Energy Electron Diffraction (LEED) and Scanning tunneling Microscopy and Spectroscopy (STM and STS respectively). This chapter aims to describe both theoretical aspects and technical implementations of the above techniques.

2.1 Low Energy Electron Diffraction

This technique allows to obtain the structural information of the samples surface. More specifically, the method is applied to check the crystallographic quality, the periodicity and the basic unit of repetition of the sample. Due to the relatively low kinetic energies (50 - 200 eV), only a few superficial layers contribute significantly to the acquired data. This can be easily understood considering the universal curve of the *Inelastic Mean Free Path* (IMFP) for the electrons (Fig. 2.1). It can be seen that in the range between 50 and 200 eV IMFP is 4 - 10 Å which corresponds, for a typical lattice constant of 2 - 4 Å, to 1 - 5 ML.

The diffraction pattern can be described with the kinematic scattering theory ([44], p. 133-147). Within this approximation the elastic scattering probability can be expressed as

$$\mathbf{W}^{(el)}_{\mathbf{k}',\mathbf{k}} = \frac{2\pi}{\hbar} N \left| f(\mathbf{K}) \sum_{p} e^{iK_{\perp} z_p} \right|^2 \delta(E' - E)\delta_{\mathbf{K}_{\parallel},\mathbf{G}_{\parallel}}, \tag{2.1}$$

where $\mathbf{k}$ and $\mathbf{k}'$ are the primary and scattered wave vectors of the electron respectively, E and E' the associated energies, $\mathbf{K} = \mathbf{k}' - \mathbf{k}$, N the number of scattering centers (i.e. atoms) per unit surface, $\mathbf{K}_{\perp}$ and $\mathbf{K}_{\parallel}$ the $\mathbf{K}$ projections

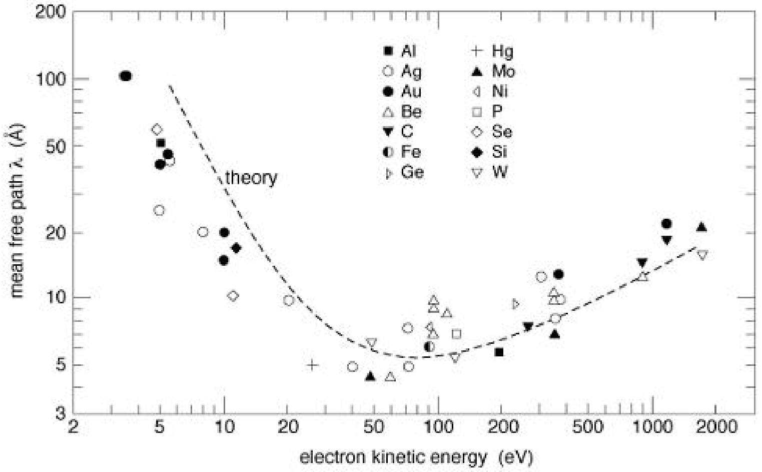

Figure 2.1: Inelastic Mean Free Path (IMFP or λ) as a function of kinetic energy (theory curve) and experimental data for different atoms (scattered points).

respectively orthogonal and parallel to the surface, z_p the distance below the surface of the *pth* plane equivalent to the surface itself, f($\mathbf{K}$) is the atomic form factor and $\mathbf{G}_{\parallel}$ the parallel component of a reciprocal lattice vector $\mathbf{G}$, defined as the vectors such that

$$e^{i\mathbf{G}\cdot\mathbf{R}_j} = 1, \quad \forall j \tag{2.2}$$

The $\mathbf{R}_j$ in the equation above is a lattice vector in direct space; it is obtained as a linear combination of three basis vectors $\{\mathbf{a}_i, \mathbf{a}_j, \mathbf{a}_k\}$ of the unit cell of the crystal.

From the Eq.2.1 it is clear that a nonvanishing contributions occurs only if $E = E'$, i.e. elastic scattering, and $\mathbf{K}_{\parallel} = \mathbf{G}_{\parallel}$, i.e a LEED pattern carry information about both crystalline order and symmetry. Note that also atomic form factor plays an important role during the LEED patter analysis, in fact some of possible scattering peaks can be hidden.

The LEED instrument used in the STM laboratory (Fig. 2.2) is composed by an LaB$_6$ crystal (electron source) wrapped by a hot filament, electron optics system (to focalize and collimate the electron beam), a series of concentric spherical grids and a spherical phosphorous screen (this geometry allows to preserve the diffracted electron direction). When the sample (positioned at the common center of screen) is invested by the beam it scatters the electrons, which travelling through the grids, impact to the screen producing a bright spot. To avoid the capture of inelastic electrons the middle grid is at the negative potential (suppressor voltage), while to guarantee a

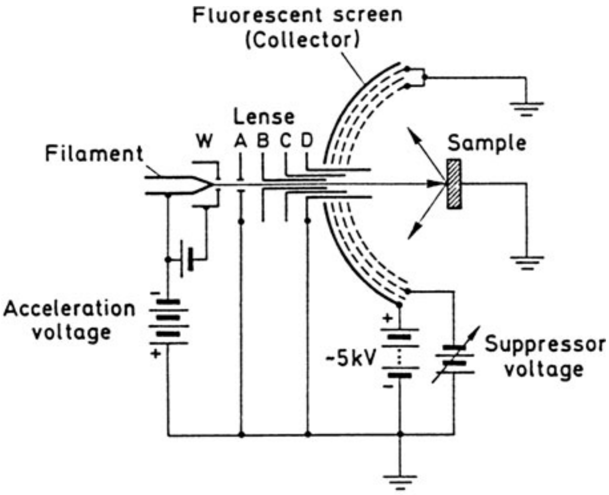

Figure 2.2: Schematic of LEED instrument.

straight elastic electron path, the other two grids are at the ground potential (as also the sample). To permit bright visible spots to the screen is applied a high voltage (about 5 keV) that accelerates the electrons to a sufficient final kinetic energy that allow to excite the phosphor.

2.2 Auger Electron Spectroscopy

Auger Electron Spectroscopy (AES) is used to characterize the chemical content of the sample and in some cases to analyse indirectly the thickness of the prepared sample. The underling physical process is Auger electron emission. When a high energy electron (primary electron) or x-ray photon imping on the sample, creates a hole vacancy generating a *secondary electron*. The atom is therefore excited and it can return to the ground state by two main processes: the core electrons can recombine either emitting a photon with a specific energy (radiative recombination) or emitting an electron from a high-lying electronic level (*Auger electron*). This electron posses a kinetic energy that is directly related to the occurred transition

$$E_{Auger}^{kin} = |\varepsilon_1| - |\varepsilon_2| - |\varepsilon_3| - \Phi,$$

where E_{Auger}^{kin} is the kinetic energy of the Auger electron, ε_1 is the energy of the hole, ε_2 and ε_3 are respectively the energy of the recombining and emitted electrons and Φ is the work function. Since the electronic levels spacing of each element is unique, from the position of the Auger peak it is possible to investigate the chemical composition of the sample. The film thickness can instead be estimated by observing the intensity decrease of the element peaks characterizing the substrate.

The instrument used for AES, in the present work, is the same as for LEED (Fig.2.2). The primary electrons are produced with a kinetic energy of 3 keV while the analysis of the *Auger electrons* is performed varying the intermediate grids potential. The acquired current (by the collector) is therefore

$$I(E) = \int_{E}^{E_p} N(\varepsilon) d\varepsilon \tag{2.3}$$

where $E = eV$ is the retarding energy and E_p is the primary beam energy.

Differentiating Eq.2.3 we obtain the $N(\varepsilon)$ spectrum but due to the relevant presence of backscattered electrons it is very difficult to distinguish peaks from the background. To avoid this problem a second derivation is performed. The above operations are accomplished by a lock-in amplifier which superimpose a small modulation δV to V. Subsequent demodulation and low pass filtering allow to obtain dN/dE.

2.3 Scanning Tunneling Microscopy/Spectroscopy

The first development of the STM instrument was done at the IBM Zurich Research Laboratory by Binnig, Rohrer, Gerber and Weibel[46](1981). The STM relies on the well known quantum tunneling effect: a particle can cross through a finite potential barrier (impossible in classical treatment) with a non-zero probability. The idea of Binnig and Rohrer was to use vacuum as the potential barrier and as a probe a sharp tungsten tip. By acquiring this tunneling current it is possible to reconstruct a direct image of the sample superficial corrugation.

Generally the STM imaging (on metals) is obtained at fixed tunneling current. While the tip scans through the sample, due to the surface corrugation the relative position z varies. As a consequence, a topography image is obtained. For electrons at the Fermi level (which contribute mostly) the surface (of the sample) represents a potential barrier whose height is the work function Φ. So in first approximation the tunneling current varies with a decay length $k = \hbar(8m\Phi)^{-\frac{1}{2}}$ [47]. For a typically parameter values we obtain $k \approx 0.4\,\text{Å}$, which corresponds to a vertical resolution of $0.1\,\text{Å}$ or better. With a good instrumental feedback it is so possible to obtain atomic resolution images. For this reason STM is useful to study directly surfaces reconstructions and symmetries. Moreover, contrary to LEED, non-periodic surfaces studies are feasible. And even when LEED and AES exhibit a clean sample surface, STM can reveal the impurities due to its better sensitivity. In the next section we will discuss briefly the theory of STM. For a complete treatment see the literature [48, 49, 50].

2.3.1 Theory

One of the main problems in the development of the STM theory is the evalutation of the real potential barrier between the sample and the tip. The Wentzel-Kramers-Brillouin (WKB) approximation ([51], p. 315-333) is adopted to this scope. A more realistic potential barrier U($\mathbf{r}$) is therefore taken instead of a simple rectangular one. The assumption of the WKB approximation is a slow spatial variation of U($\mathbf{r}$) with respect to the characteristic spatial scale of the particles involved, i.e. their De Broglie wavelength.

Using a WKB approximation within a first-order time-dependent perturbation theory, Bardeen [52] assumes that electron-electron interaction can be ignored, occupation probabilities for the tip and sample are independent of each other (and do not change despite the tunneling) and the tip and sample are in electrochemical equilibrium. Within this approximations the tunneling current can be expressed as

$$I = \frac{2\pi e}{\hbar} \sum_{\mu,\nu} f(E_\mu)\left[1 - f(E_\nu + eV)\right] |M_{\mu\nu}|^2 \delta(E_\mu - E_\nu), \tag{2.4}$$

where $f(E)$ is the fermi function, V is the applied voltage, $M_{\mu\nu}$ is the tunneling matrix between state ψ_μ of the probe (tip) and ψ_ν of the sample surface and $E_{\mu,\nu}$ are the respectively states in absence of tunneling. Contrary to the perturbation theory ψ_μ and ψ_ν are related to different hamiltonians, which means that they are non-orthogonal. For high temperatures there is a corresponding term for reverse tunneling. Despite the apparent simplicity, in this expression the critical part is the matrix element [52]

$$M_{\mu\nu} = \frac{\hbar^2}{2m} \int_S (\psi_\mu^* \nabla \psi_\nu - \psi_\nu \nabla \psi_\mu^*) \cdot \mathbf{n} d\sigma, \tag{2.5}$$

where the integration is taken along a surface S lying in the barrier region with normal unit vector $\mathbf{n}$. Note also that the integrand is equivalent to the density current operator. A priori we don't know the expressions of the states involved in tunneling, so further approximations must be done to evaluate the matrix element.

To understand the meaning of the tunneling current we can consider a simple case of ideal point probe and low temperature (even at room temperature) and small voltage (∼10 mV). If the tip wave functions are arbitrarily localized, then the matrix element is simply proportional to the amplitude of ψ_ν at the position $\mathbf{r}_0$ of the probe, and 2.4 reduces to [47]

$$I \propto \sum_{\nu} |\psi_\nu(\mathbf{r}_0)|^2 \delta(E_\nu - E_F), \tag{2.6}$$

where the quantity on the right is the surface local density of states (LDOS) at E_F. This simple result explains the meaning of the microscope image which is a contour map of the constant surface LDOS. To avoid the sum in 2.4 and 2.5 we introduce the tip and sample density of states, ρ_t and ρ_s respectively, to obtain

$$I = \frac{2\pi e}{\hbar} \int_{\Re} T(z, E, V) \left[f(E) - f(E - eV) \right] \rho_s(E) \rho_t(E - eV) dE, \tag{2.7}$$

where z is the tip-sample distance and $T(z, E, V)$ (transmission coefficient) has been defined as the average value of $|M_{\mu\nu}|^2$ over the states whose energy lies in small energy interval δE. The tunneling current is thus related via the transmission coefficient and the Fermi function to the so-called joint density of states of sample and tip. The barrier geometry is defined by the applied voltage V and by the average of the work functions of the sample and the tip, $\phi = 1/2(\phi_s + \phi_t)$, thus the transmission coefficient can be expressed as [53]

$$T(z, E, V) = exp \left[-\frac{2z}{\hbar} \sqrt{2m(\phi - E + \frac{1}{2} eV)} \right], \tag{2.8}$$

where m is the mass of the electron. We can observe that the tunneling current depends exponentially on the tip-sample distance and on the barrier height. As a consequence, changing z by a small value (e.g. 1 Å) the current drops down (or increase) significantly. And since the barrier height is referred to the vacuum level, electrons close to the Fermi level thus contribute mostly, as can be seen in Fig. 2.3. The resulting STM image is a topographic representation of the sample superimposed by a modulation caused by the electronic structure.

Another important aspect must be considered. Even if the first atomic layer contribute to the tunneling current of about 90%, also the second and eventually the third can contribute, especially when the tip-sample distance is small enough [47]. In this way large (at least (3x1)) superficial reconstructions can be investigated.

As we have seen in Eq.2.7, $\rho_s(E)$ ($\rho_t(E)$ is generally considered as a constant) plays an important role in STM microscopy. Thus the electronic structure of the sample can be investigated varying tip-sample distance, which

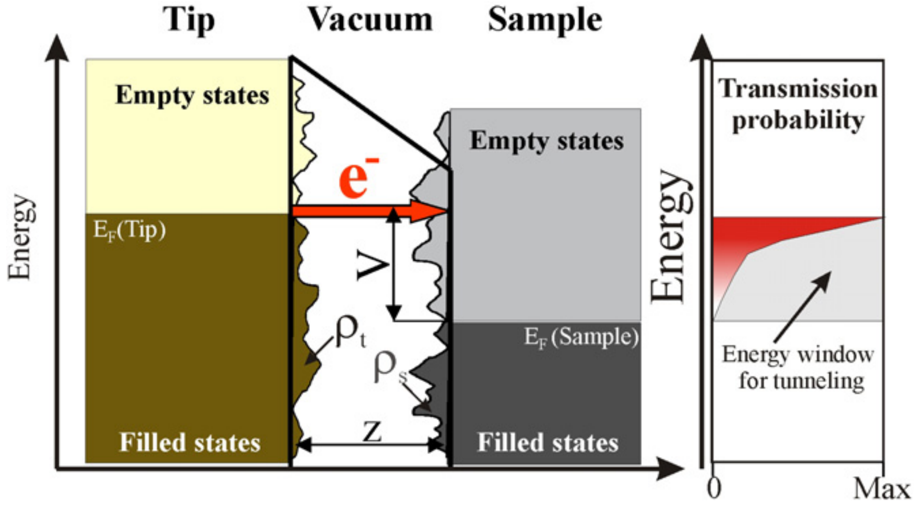

Figure 2.3: Sketch of the energy-dependent tunneling probability across the tip-sample distance (left) and potential diagram of junction (right), [45].

means (in constant current microscopy) changing the voltage V or the tunnel current I. In the first case more or less electronic levels are involved. In the last case are varied the relative contributions of the states in the first Brillouin zone, i.e of the orbitals. Indeed for large z values the tunneling current is essentially determined by the $\overline{\Gamma}$ states whose decay length is the longest. Despite of this possibility to investigate the electronic states and energy spectrum of the sample with a topographic analysis, a more detailed and immediate method can be implemented: Scanning Tunneling Spectroscopy (STS). A voltage ramp is applied to the sample and the respective current is acquired. More in detail, through a lock-in amplifier, the acquired data is dI/dV. To understand the physical meaning of such operation we derive Eq. 2.7 and obtain the following

$$\begin{aligned}\frac{dI}{dV} =& \frac{2\pi e}{\hbar}\int_{\Re}\left[f(E)-f(E-eV)\right]\rho_s(E)\left[\frac{\partial T(z,E,V)}{\partial V}\rho_t(E-eV)\right.\\ &\left.-eT(z,E,V)\left(\frac{\partial\rho_t}{\partial E}\right)_{E-eV}\right]dE \\ &-\frac{2\pi e}{\hbar}\int_{\Re}T(z,E,V)\rho_s(E)\rho_t(E-eV)\left(\frac{df}{dE}\right)_{E-eV}dE.\end{aligned} \tag{2.9}$$

If we considerate for simplicity the case of the low temperature limit, the

Fermi function becomes a step function and the equation above becomes

$$\begin{aligned}\frac{dI}{dV} =&\frac{2\pi e}{\hbar}\int_0^{eV}\rho_s(E)\left[\frac{\partial T(z,E,V)}{\partial V}\rho_t(E-eV)-eT(z,E,V)\left(\frac{\partial \rho_t}{\partial E}\right)_{E-eV}\right]dE\\ &+\frac{2\pi e}{\hbar}T(z,V)\rho_s(eV)\rho_t(0).\end{aligned} \tag{2.10}$$

For low bias we can consider both the density of states of the tip and the transmission coefficient to be independent of V. This means that only the last part in Eq.2.10 is relevant. Within this approximations we obtain

$$\frac{dI}{dV}=\frac{2\pi e}{\hbar}T(z,V)\rho_s(eV)\rho_t(0). \tag{2.11}$$

Finally we can see that dI/dV is the LDOS of the sample at the energy eV from the Fermi level modulated by the transmission coefficient. So introducing an appropriate ramp of voltage we can explore the respective electronic structure of the sample. The LDOS of the tip (at the Fermi level) is only a proportional coefficient and do not interfere, if the approximations above are correct, to the acquired spectrum.

2.3.2 STM Apparatus

As we have seen the tunneling current depends exponentially on z (tip-sample distance). Consequently, to achieve an STM image or STS spectra the setup must be extremely stable in order to control the distance up to 0.05 - 0.1 Å which guarantees a stable current of 10 pA - 50 nA. To avoid the inevitable mechanical vibrations (which determine the resolution) the STM is fixed on a rigid circular stage attached to four spring whose resonance frequency is about 2 Hz. Moreover there is a series of copper plates partially immersed in the magnetic field generated by permanent magnets. When the system start to oscillate the magnets induce an eddy current in the plates which in turn generates an opposed magnetic field. As a consequence, the oscillations are damped. Another problem is the approach of the tip to the surface and its movement during a scan. Typically the scanned areas are about 10 nm^2 - 1 μm^2. For this purpose piezoelectric (PZT) actuators are used. The approach of the tip is performed with a combination of a linear piezodrive, for relatively large movements, and a piezo tube elongation, for a fine z positioning. During the image acquisition is used a PZT which can bent in the parallel directions (with respect to the sample surface) and elongate along its axis to adjust the tip-sample distance.

The topographic image can be achieved with two mechanisms: *constant absolute position* and *constant current*. In first case the absolute normal position of the tip is kept constant while the tunnel current I is acquired during raster-scan mechanism. Behaviour changes are reconstructed with a false color map. The former scanning mode can be performed on large flat structures but when a step occurs the tip can crush on it, so some precautions might be done. In the second case, the tip is moved even in its axis to maintain a constant tunnel current. If we neglect the LDOS modulations, in this case the relative distance z is kept constant, which is true for a conductive materials but it's more complex for semiconductors and isolators (e.g oxides which will be discussed in the next section). In the *constant* I mode the use of a feedback mechanism is required to adjust the tip-sample distance. As a consequence the image performing might be done slowly to achieve a correct experimental result.

To obtain a spectra, first of all it has to be chosen a set-point. In a *constant current* mode, voltage and current are set and the feedback mechanism is turned off, so the tip is held in the same position and z distance in respect to the sample.

Up to now nothing has been said about the tip. First of all it must be metallic to permit a conductance for all bias voltages (of the sample): for $V > 0$ empty states of the sample are investigated, while for $V < 0$ the occupied ones. Furthermore magnetic tips might be used to study the magnetic properties of the sample [54]. In the STM lab is used usually a W (tungsten) tip. To obtain a sharp, ideally one-atom terminated, tip an electrochemical etching is performed. A small part of the W wire (~5 mm) is positively DC biased with respect to a circular gold wire (cathode) on which is present a bubble of 2 M NaOH solution, formed as a result of surface tension. The etching process takes place preferentially on the curved air-electrolyte interface resulting in a progressive necking of the wire.

2.3.3 STM/STS On Nanostructured Oxides

Oxides are generally low conductive materials due to the presence of conductive-valence band gap and a small charge (electron or hole) mobility. As a consequence STM analysis is not always possible even with sample bias out of band gap. On thick (~10 nm) bulk oxides, charging effects can compromise measurements, which become reliable only with sufficient concentration of dopant. A metal support is useful to limit charging effects and, for thin samples, to permit working even at low bias (i.e. in the middle of the gap). In general STM investigation on oxide is possible if one of the following conditions is fulfilled [45]:

- There is a sufficient intrinsic density of carriers even at low temperature.

- Metal electronic states overlap, trough the oxide, with those of tip permitting tunnel current both for narrow as wide gap materials. This is only possible for ultra-thin films of about $5 - 10\,\text{Å}$ thickness.

- For high voltages (5 - 15 V), due to the formation of the quantization states in the vacuum (field emission resonaces [55, 56]), ballistic injection of electrones into the conduction band is possible. As a consequence thicker (up to 50 Å) oxide can be investigated. However the spatial resolution is reduced [57], as will be discussed afterwards.

- There is a sufficient density of carriers with a high sample temperatures. Note that due to heating oxygen can desorb, leaving two electrons and thus doping the oxide [58].

- As anticipated above, a carrier concentration can be increased with an intrinsic dopant effect, like oxygen vacancies or impurities. The resulting electrons states in the gap can thus populate the conduction band. This works well for narrow gap oxides and less for wide ones.

- Conductive surface states can be formed under molecular species adsorption or metallization with H [59].

When STM is possible for one of the above reasons, the interpretation of results may be quite different from those of metal samples. For bias in the gap the apparent height may be governed by the metal-oxide junction, which produces states with long decay length, or by spatial-varying electronic properties induced by defects (impurities, step edges, oxygen vacancies, adsorbates) [60]. Instead for bias close to the onset of bands (conduction or valence) electron (hole) transport become available in the oxide. As a consequence, a drastic increase of height in topographic image is detected. By varying the bias in the range containing the gap, with a topographic analysis the gap size could be estimated [36, 61, 62]. At large sample bias, however, the image contrast can be governed by the transmission coefficient (Eq. 2.8) which become strongly dependent on the confined vacuum states mentioned before [55, 56], more than by the tunneling probability. As a consequence the transport of these states become governed by the local work function modulation more than by the topography [63]. Another difference between metal and oxide samples should be considered. For metal the assumption made in STM is that the applied voltage across the sample-tip junction is dropped within the vacuum because of the high density of "free" electrons. For low conductive materials instead, such screening is no more possible and the penetration of the electric field influences the STM study. The size λ of the screening region can be estimated using Poisson's equation. Neglecting the minority charge carrier the solution is [57]

$$\lambda = \left(\frac{2\varepsilon kT}{q^2 N}\right)^{\frac{1}{2}} \tag{2.12}$$

where ε is the dielectric constant of the sample, k is the Boltzmann constant, T is the temperature (in Kelvin), q is the elementary charge and N is the number density of charge carriers. We can see that if the charge density increases, λ decreases. For oxides, where the charge density is small, λ become relevant and the STM atomic resolution can be compromised. Another aspect of electric field penetration is the bending of both conduction and valence band influencing the STM measurement [64, 65, 66, 67]. The amount of band bending depends on the applied voltage, on the oxide thickness d and on dielectric constant ε. To estimate its value, we can approximate the tip-sample junction as a capacitor filled partially with a dielectric medium. If z is the tip-sample distance we define $\eta = d/z\varepsilon$ as the ratio between the voltage drop inside the oxide and the total junction (vacuum and oxide). The shift of the band onset from flat-band position E_0 is therefore [64]

$$\Delta E = E_0 \left(\frac{\eta}{1-\eta}\right). \tag{2.13}$$

Despite this expression highlights that the amount of band bending decreases if the tip-sample distance increases or the thickness of the oxide decreases, it does not take into account of voltage dependence. Indeed, by increasing voltage, the band bending becomes more pronounced. Moreover, band bending depends even on the sign of voltage. As a consequence the evaluation of gap size with STS spectra is intrinsically overestimated.

For what regards spectroscopy, STS captures only those states that overlap sufficiently strong with the tip wave functions. It was calculated that mostly the s-like and p-like states contribute in conductance spectra while the d-like and f-like states, due to the more localized behaviour, are hardly detectable [68].

Chapter 3

Experiment And Discussion

3.1 Substrate Preparation

The starting sample is a $160\,\mu$m thickness MgO(001) single crystal of $1\,\mathrm{cm}^2$ in size. For the experiments, it is fixed on a Ta sample-holder. To obtain a clean surface of such substrate various annealing cycles was performed under UHV conditions. Successively 500 nm of Fe was deposited using the MBE technique. Initially iron grows on MgO(001) with an ordered c(2x2) structure. Successive relaxation occurs, resulting in a (001) exposed surface of body-centered cubic (bcc) bravais lattice. Because of high thickness, bulk structural parameters are obtained at the surface resulting in 2.866 Å of the cubic unit cell.

This iron thick layer is, in turn, used as substrate for the other samples. To prepare a new sample ion-bombardment sputtering procedure is adopted. In our case a contaminants free surface is obtained after $5'$ of sputtering at $10\,\mu$A. Successive annealing at 500 °C for $10'$ serves to obtain a well defined non defective surface. After exposition to 30 L of oxygen at $2{\cdot}10^{-7}$mbar, at the same temperature, and additional annealing (600 °C for $10'$) a well ordered oxygen saturated structure is reached. The latter heating serves to remove excess of chemisorbed oxygen. As a result, the well characterized Fe(001)-p(1x1)O surface is obtained, where one oxygen atom per in-plane unit cell is located in fourfold hollow sites of the surface [69].

Such a substrate presents large flat terraces, as could be seen from the STM image in Fig.3.1 (a). From LEED pattern (see inset), a (1x1) symmetry is confirmed, and the brightness of the spots suggest a well ordered surface structure. In the image, it is also observed a 16 ML[1] high Fe step (Fig.3.1 (b)). Generally, on this substrate, the majority of steps are high several

---

[1] 1 ML = 1.433 Å.

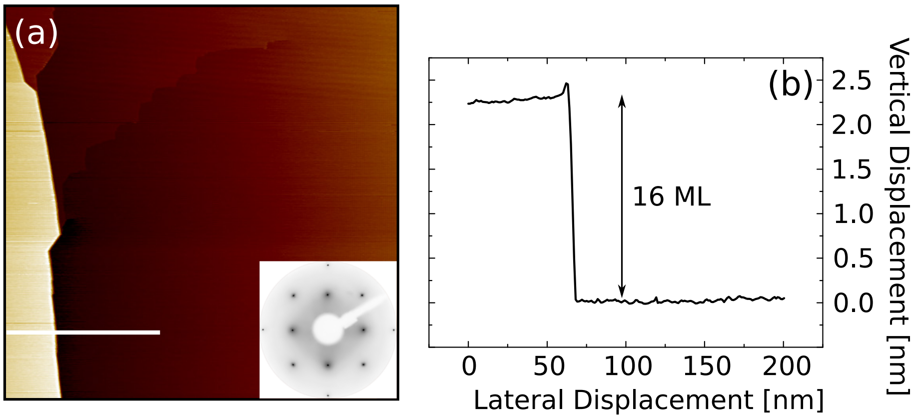

Figure 3.1: (a)-STM image and LEED pattern (inset) on Fe(001)-p(1x1)O surface. (b)-Topographic profile of the step (white line in panel (a)).

atomic planes, only about 5% are found to be monoatomic.

A cobalt thin film of nominally 5 equivalent monolayers[2] (ML) was deposited at room temperature using MBE. A flux of 0.9 Å⁄min was measured with the quartz micro-balance. Successive annealing at 200 °C for $10'$ was performed. During the sample preparation, the pressure was stable at about $p{\sim}2{\cdot}10^{-10}$mbar.

STM images and AES spectra, of the 5 ML of Co on Fe(001) sample, were acquired before and after annealing. Before heating the sample, high roughness surface (Fig.3.2(a)) with a successive layer nucleation sites is detected. After 200 °C (Fig.3.2(b)) a flat surface is formed with large holes due to the not perfect completion of the last layer. In both cases, holes are found to be depressed with respect to the uppermost layer by about 140 pm (panels (c) and (d)) which is consistent with 1 ML height of the cobalt (143.3 pm). A perfect layer-by-layer growth mode is thus observed. From LEED analysis (not shown) is also verified the registry growth of cobalt with respect to the iron substrate. In fact a (1x1) LEED pattern is observed before and after 5 ML deposition and also after 200 °C annealing. This results confirm that a metastable bct (body-centered tetragonal, see later discussion) Co phase develops in the first monolayers. The main importance of having a large flat substrate is that the successive oxide development is expected to form a regular structure, with respect to the defective surface where oxide grows predominantly close to the step edges.

---

[2] One equivalent monolayer is calculated as the amount of Co needed to completely cover the Fe substrate. The thickness of 1ML is half the cubic lattice parameter of Fe bcc structure, i.e 1.433 Å.

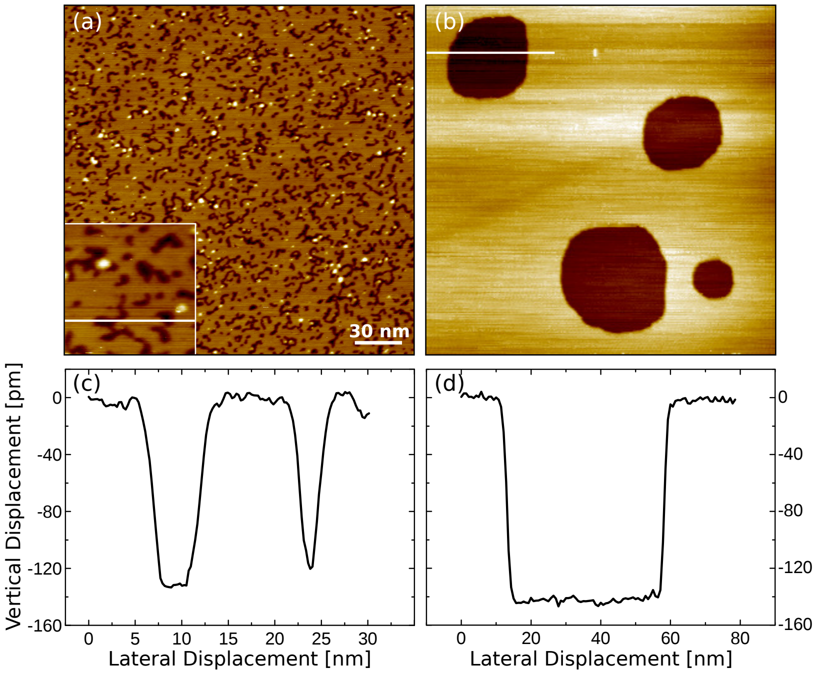

Figure 3.2: STM images of 5 ML of Co on Fe(001)-$p(1x1)$O oxygen saturated substrate. After deposition of cobalt at room temperature (a); after the sample has been heated at 200 °C (b). The size of images are 200x200 nm^2. In both images last layer is quite complete and the vertical displacement of the holes, (c) and (d) respectively is compatible with one ML height. Panel (c) is referred to the inset of panel (a).

Oxidation of the cobalt film is obtained exposing the sample to oxygen at 200 °C. Up to 100 L the used partial pressure of oxygen was $2{\cdot}10^{-8}$ mbar, while up to 120 L a higher value ($2{\cdot}10^{-7}$ mbar) is adopted. Further annealing for $5'$ at the same temperature is performed to promote diffusion and removal of exceeded oxygen.

3.2 Chemistry of the Oxidized Co Film on Fe(001)

From the AES data at high energy (Fig.3.3(a) and (b)) it is clear that oxygen KLL and cobalt LMM peaks do not vary significantly. This suggests that cobalt does not intermix further, with the underlying iron, at 200 °C, but initial intermixing is not excluded. Moreover we can observe that $p(1x1)$ oxygen on cobalt does not desorb significantly after annealing. As a result, a oxygen-rich substrate is formed which has the scope to promote the oxide growth. In addition, from the AES data at low energy (Fig.3.3(c) and (d)), there is not evidence of iron floating to the surface, especially at grazing

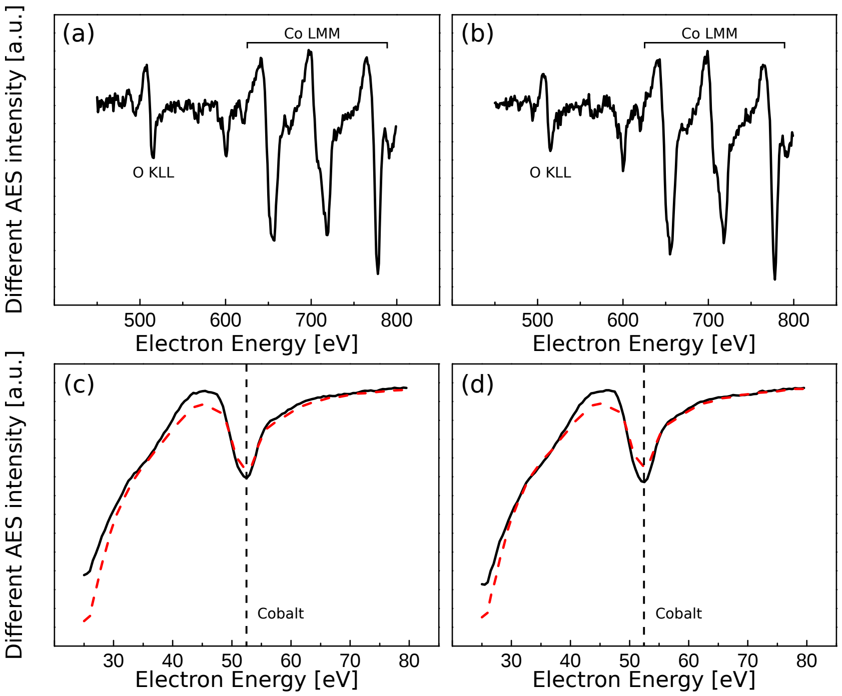

Figure 3.3: AES data relative to the range of oxygen and cobalt, (e) and (f), and in the low energy range for normal (straight black curve) and grazing (dashed red curve) incidence, (g) and (h).

incidence, where only the cobalt peak is observed.

In Fig.3.4 AES data are shown before and after the oxidation of 5 ML of cobalt. Iron LMM peaks are clearly visible on Fe(001)-$p(1x1)$O sample (curve (i)) and upon further 50 L (curve (v)) exposition of oxygen on iron substrate. The characteristic iron oxide peak is visible on this spectra (Fig.3.4 (b)). Clearly, after iron oxidation its intensity is higher. After cobalt deposition and successive oxidation with total 20 and 500 L (Fig.3.4 (b), curves (ii)-(iv)), the iron oxide peak is not present and the metallic peak is suppressed. After cobalt deposition, the iron peaks in the AES high energy data, are decreased in intensity and only one of them is visible. With successive oxidations there is not any significant variation of this iron peak (at 598 eV), while at low energy (47 eV peak) it seems that a small intermixing occurs. At low energy the development of the cobalt oxide peak ($\sim$42 eV), between iron oxide and iron peaks, compromises the identification of either iron intermixing or iron oxidation on the surface. As a consequence, iron presence close to the

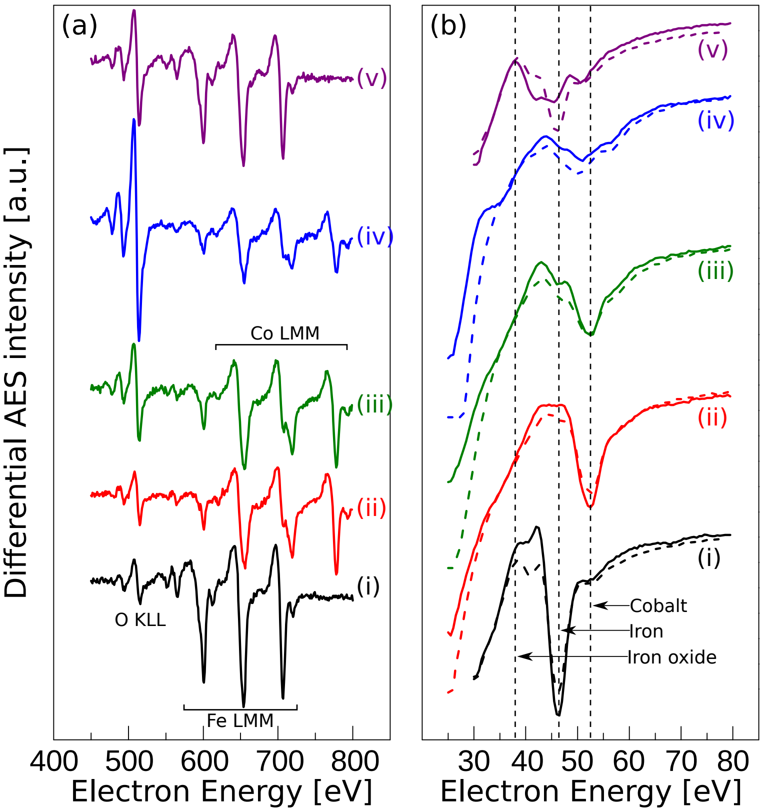

Figure 3.4: AES spectra at high energy (a) and low energy (b) at normal and at grazing incidence (panel (b) dashed curves). From the bottom are shown Fe(001)-$p(1\text{x}1)$O substrate (i), with additional 5 ML of cobalt at room temperature (ii), after total 20 and 500 L of oxygen at 200 °C ((iii) and (iv) respectively) and for comparison 50 L on Fe(001)-p(1x1) substrate (v).

surface can be neglected also because of the grazing[3] spectra (Fig.3.4 (b), curves (ii)-(iv)), which do not suggest iron presence but clearly highlight the decrease of metallic cobalt and the development of the cobalt oxide. This is also confirmed in the correspondent spectra at high energy (Fig.3.4 (a), curves (ii)-(iv)), where the oxygen peaks clearly increase in intensity and the cobalt ones decrease visibly after 500 L. As a result, we can consider that predominantly cobalt oxide forms, while the iron substrate is not influenced by the presence of oxygen in the first few monolayers close to the interface.

---

[3] Grazing spectra are more sensitive to the surface because of the high incidence angle (∼73°), which decreases the escape depth of the electrons with respect to the surface. Escape depth is the maximum depth (measured from the surface) at which there is a high probability that the electron could escape from the sample without loosing its information (i.e. the specific kinetic energy).

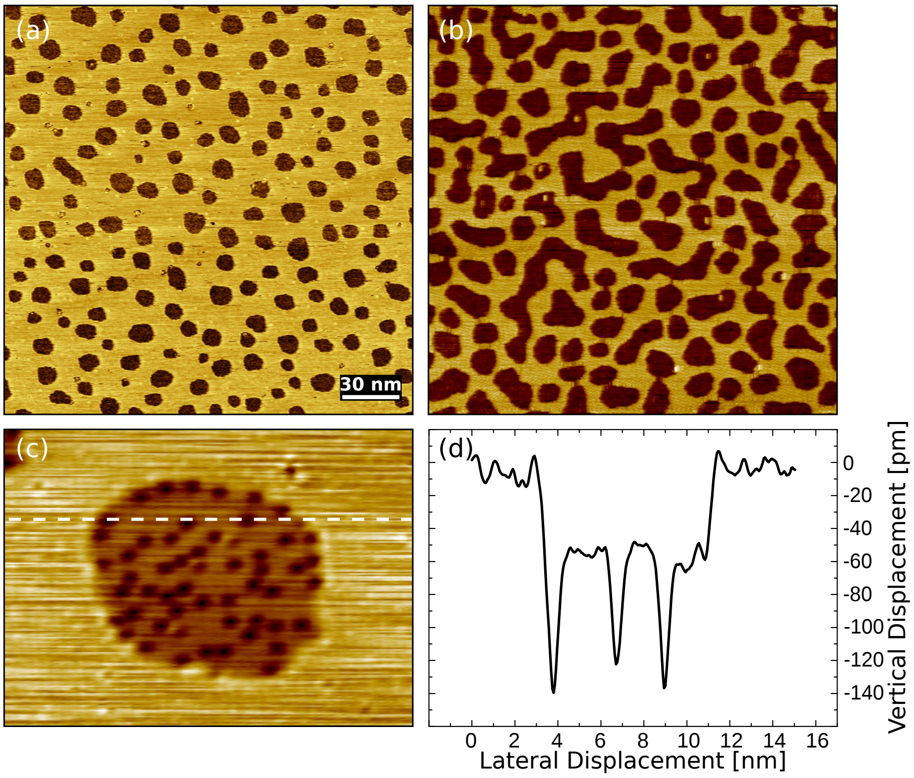

Figure 3.5: STM images (200x200 nm^2) of the first stages of oxidation: after 2 L (a) and 7 L (b) of oxygen (200x200 nm^2). The tunneling parameters are 1.1 V, 1 nA and 1 V, 1 nA respectively. Panel (c) shows more in detail the oxide zone at 2 L (tunneling parameters are 1 V, 1 nA) with the respective profile in panel (d).

3.3 Early Stages of CoO Formation

The development of the early stages of cobalt oxidation is visible in STM images (Fig.3.5). For 2 L (panel a), one can identify the cobalt substrate, on which oxygen is chemisorbed, and the oxide region which develops in relatively large ($\sim$ 10 nm of diameter) rounded shape islands. On the oxide regions, quasi-uniformly distributed dark spots can also be seen (Fig.3.5 (c)). For tunneling parameters of such an image (1 V, 1 nA) oxide islands are seen as depressions, with respect to the substrate, by 60 pm while dark spots are depressed by about 140 pm (Fig.3.5 (d)).

The latter data must be interpreted with caution. In fact, while STM on metals gives "more directly" information on the sample topography, for studies on oxides the electronic gap and low charge mobility must be considered (for more details see subsection 2.3.3). As a consequence even if the oxide topography is depressed, it could not be concluded that it is embedded in the substrate because tunneling through the oxide could have been occurred.

Exposing the sample to further 5 L (7 in total) the coalescence of the oxide islands is observed (Fig.3.5 (b)), i.e. the number of the islands decreases while their dimension increases. Cobalt oxide thus develop in layer-by-layer growth mode on the flat cobalt surface. Conversely, on the step edges (not shown) the oxidation is faster and the second layer grows before the completion of the first one. As a conclusion, a large flat surface is preferred in order to control the cobalt oxide growth mode.

The dependence of the oxide STM data with respect to the tunneling parameters (especially on the applied voltage) is presented in Fig.3.6. Dual scan mode is adopted on the same acquisition: the forward scan is performed at voltage of 1.5 V and tunneling current of 10 pA, while the backward scan is done at voltage of 1 V and tunneling current of 450 pA. Contrast inversion of the image is observed because of the different position of the Fermi level of the tip with respect to the oxide states. In the first case (Fig.3.6 (a)) tunneling parameters are sufficient to detect the conduction band of the oxide, and the relative height, with respect to the cobalt substrate, is positive, as can bee seen in the histogram on the right of the image. The histogram, of a specific STM image, is obtained by calculating the relative frequency of the pixels' topographic heights. Conversely, in the second image the tunneling parameters are such that they don not permit to tunnel in the oxide states. As a result, tunneling occurs through the island and the relative height is negative with respect to the substrate (see the respective histogram). Note that a perfect contrast inversion occurred for such tunneling parameters: 84 pm with respect to -85 pm (see Fig.3.6).

To understand the dependence of the oxide relative height with respect to the tunneling parameters, various measures were performed varying both the applied voltage and the tunneling current. Changing the former allows to obtain an indirect information of the electronic structure and especially the gap size. While changing the latter, at fixed voltage, information about the wave function[4] dependence with respect to the distance from the sample to the tip, can be obtained. The above data were acquired in dual mode taking fixed the forward scan (1.5 V and 10 pA) and varying the backward tunneling parameters. For every voltage, from -2 V to +2 V with a step of 0.4 V (except around zero, that can not be measured, where the steps were of ±0.2 V) different images were acquired changing the tunneling current from 50 pA to 500 pA whit steps of 50 pA. The forward scan was necessary to perform a comparison between different images, because of the observed dependence of

---

[4] More specifically it is the overlap of the sample and tip wave functions.

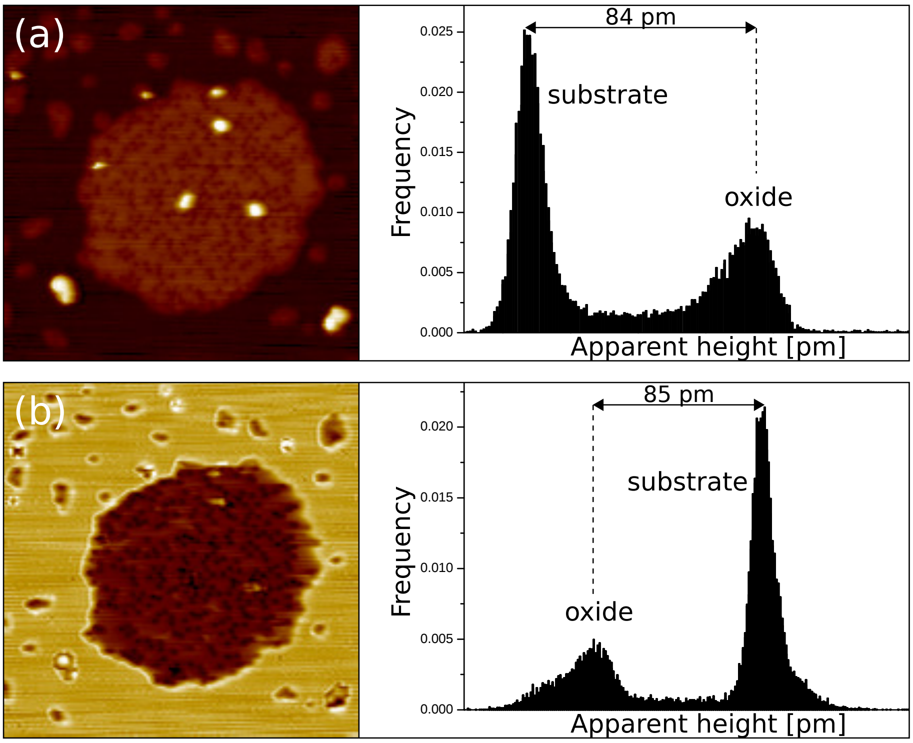

Figure 3.6: STM images acquired in dual mode on the same region (34x34 nm^2). Forward scan (a) was done at 1.5 V, 10 pA, while the backward (b) at 1 V, 450 pA. On the right of both images, apparent height histograms are presented as a function of the vertical height of the oxide islands with respect to the cobalt substrate. The sample was prepared exposing 5 ML of Co/Fe(001)-p(1x1)O, to 10 L of oxygen.

the relative oxide height from the different states or conformations of the tip. In fact various data were acquired with the same tunneling parameters but with quite different relative heights. The selected data on which the check measure (forward scan) was stable (error bar of about 20 pm) were plotted in the level curve graph (Fig.3.7 (a)). It should be noted that the range of values of the relative height is relatively large.

A simple evaluation of the electronic band gap can be obtained with height analysis of the data. In first approximation, the band edges should be placed where the oxide height, with respect to the substrate, crosses the zero-height level (red dashed curve in Fig.3.7 (a)) [36]. To justify this argument we have to distinguish the situations when the tunneling process occurs in the gap or out of it. When the Fermi level of the tip is situated in the gap, tunneling in the oxide material is not possible if there is no energy levels produced by contaminants or by the coupling at the interface with the

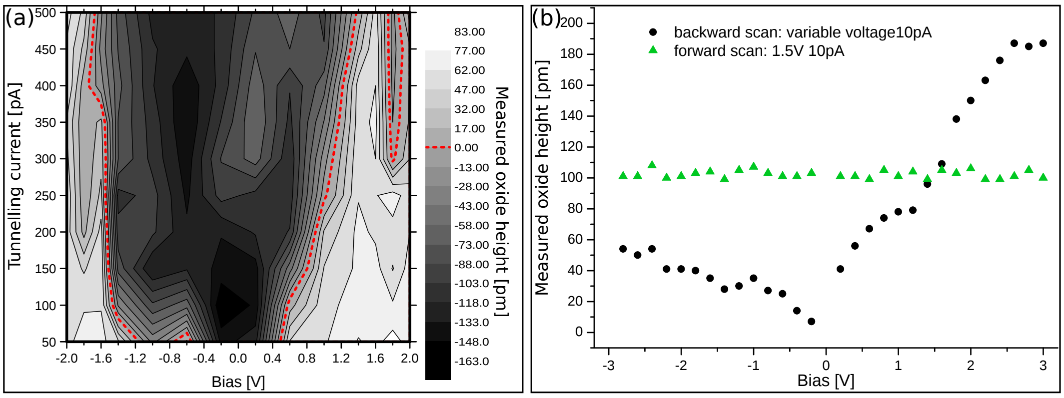

Figure 3.7: (a)-Level curve graph of the relative height of the oxide islands as a function of the applied voltage (from -2 V to +2 V) and tunneling current (from 50 pA to 500 pA). The red dashed curve is the zero-height level. (b)-Measured oxide height in dual mode with forward fixed at 1.5 V and 10 pA (green triangles) and backward with variable voltage and fixed current (black circles).

underlying metal. As a consequence, the oxide is depressed with respect to the substrate in the STM images. On the other hand, if the Fermi level is above the minimum of the conduction band (or below the maximum of the valence band) tunneling in the oxide is expected if the density of states is enough to reach the specific current. In this case the, oxide should be observed as protruding islands. Thus, neglecting the electronic states in the gap and the possible low density of states at the edges of the bands (and also the low charge mobility) we can evaluate the gap size from the zero-height level.

We can observe that the gap size does not remain constant (Fig.3.7 (a)). The valence band edge in first approximation is constant at -1.6 eV (varying from -1.7 eV to -1.2 eV) while the conduction band edge is at about 1.4 eV for 500 pA and 0.5 eV at 50 pA. As a result the gap size changes from 1.7 eV to 3.1 eV. In Fig.3.7 (a) we can also observe that the relative height crosses again the zero level at 1.8 V for high tunneling currents. But this feature is interpreted as experimental error and does not change the physics of the system.

Even if the bulk cobalt oxide gap (2.5 eV) was in the middle of the above values, the resulting high variation is not acceptable. The reason of such uncertainty might be in the approximation adopted. First of all we can observe that in the gap region (Fig.3.7 (a)) the relative height does not remain constant but changes for about 100 pm after the rapid fall. Thus states in the gap are present. These might be referred to the dark spots, if they are oxygen vacancies, and/or to the coupling of the oxide at the interface with the metal. This consideration is supported by the data exposed in Fig.3.7 (b) that are acquired at 10 pA tunneling current, either varying the voltage (black circles), or taking the voltage fixed at 1.5 V (green triangles), which serves to control the stability of the tip. It should be noted that none of the data crosses the zero level, resulting in the apparent absence of the gap. Anyway, one cannot conclude to have a metallic surface because STM on metals does not produce such large height variations with respect to the applied voltage. In addition there is a raise in the height for positive voltages up to a plateau at about 200 pm for 2.4 V, while for negative voltages the maximum value is about 60 pm.

Another approximation adopted is supposing the high density of states at the edges of the electronic bands. If this was the case, the relative height must rapidly reach the topographic value and maintain it for every other higher (in modulus) applied voltage. In our measurements, we do not observe such a trend. To obtain an accurate information on the density of states, STS analysis was performed on oxide islands and on the substrate (in order to confirm the metallic behaviour). The obtained I-V curves are plotted on a logarithmic scale in order to detect region with low density of states (Fig.3.8). In fact, if the argument goes to zero the logarithm decrease rapidly to a high negative value. As a result, the band edges can be observed because the conduction, in the ideal case, is zero. Due to the noise, the zero conductance is never reached but the data present an oscillating behaviour around zero where the density of states is zero, i.e. in the gap. We can observe (Fig.3.8) that the substrate clearly has a metallic behaviour presenting a symmetry with respect to the zero voltage. On the other hand, the oxide presents a higher density of states for positive voltages (i.e. in the conduction band) than for negative ones (i.e. valence band).

To obtain an estimation of the gap size, the detection limit (horizontal dashed line in Fig.3.8) is used to distinguish the noise from the real data. The resulting values for the valence and conductance edges are respectively -1.5 eV and 0.8 eV. As a result, a 2.3 eV gap is obtained, which is consistent with the bulk one [31]. Note that the real gap value can be smaller because of the band bending induced by the tip voltage (see subsection 2.3.3). Another observation is that the Fermi level of the oxide might not be in the middle of the gap as for the bulk crystal. The shift is of 0.35 eV toward the conductance band (Fig.3.8). As a consequence, the oxide presents n-type behaviour. The reason might be attributed both to the surface localized charges, because of the oxygen vacancies (F centres), and to the Schottky barrier at the interface between metallic cobalt and cobalt oxide, which produces a charge transfer. In both cases, due to the low screening capability of the oxide, the local-

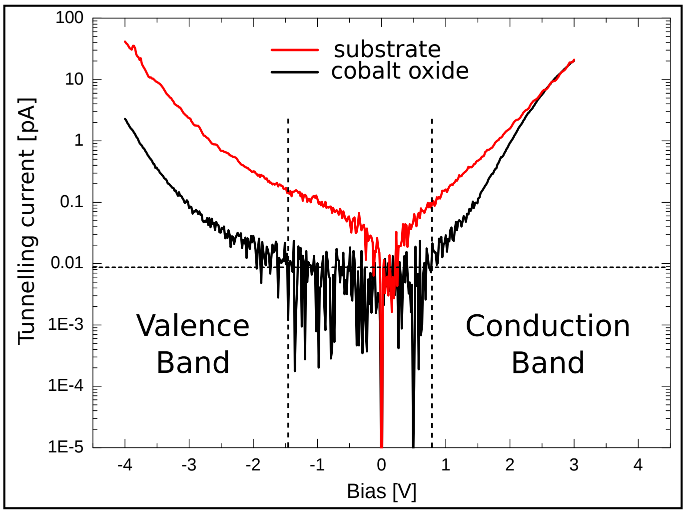

Figure 3.8: STS I-V curves on the cobalt substrate (red curve) and on the cobalt oxide region (black curve) plotted in logarithmic scale. Spectra were acquired from -4 V to +3 V with set point of 2.8 V and 10 pA. Dashed horizontal line represents the upper detection limit while the vertical dashed lines represents the estimated band edges.

ized charges produce a band bending which is extended through the oxide because of the low thickness. If the reason was only the charge transfer at the interface, increasing the oxide thickness this phenomena would gradually vanish at the surface where the bulk-like characteristic should be detected (i.e. the band edges values symmetric with respect to the zero voltage) [45]. In our case, due to the low oxide thickness, it was not possible to confirm this statement.

One of the main problems to evaluate the gap size was placing the edge of the valence band. The phenomena is represented schematically in Fig.3.9. In this model, the transmission function (Eq.2.8) plays an important role. For a given applied voltage V, the shift between the Fermi level of the tip and that of the oxide is equal to eV. Thus, if the Fermi level is above the minimum of the conduction band (panel (a)) or below the maximum of the valence band (panel (b)) tunneling process in the oxide occurs. The number of the transmitted electrons (bright red arrows) is different in the two cases. In fact, even if the tip Fermi level is only slightly above the minimum of the conduction band, on account of the trend of the transmission function (see the right panel of Fig.2.3), a high conductance is expected. The same is not true if the tip Fermi level is slightly below the maximum of the valence band where the transmission function have its minimum value. In the latter case, a higher voltage (in modulus) must be applied to detect a relevant

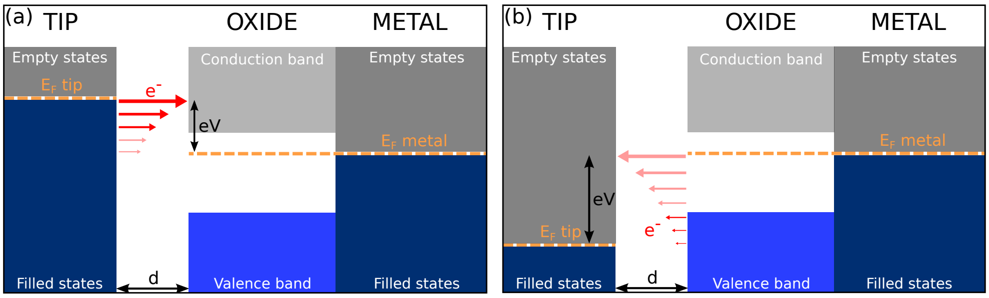

Figure 3.9: Schematic representation of the tunneling current for applied voltages (V) above the conduction band minimum (a) and below the valence band maximum (b). The sample-tip distance d is kept constant. The red arrows are referred to the tunneling electrons. The different colors are referred to the tunneling in the oxide levels (bright red) and through the oxide in the cobalt substrate levels (light red). The size of the arrows represents the number of tunneling electrons, i.e. the transmission probability.

contribution of the valence band. Moreover, a small contribution to the tunneling current is given by the tunneling in the underlying cobalt through the oxide island. This contribution is higher for the valence band than for the conduction band (see the light red arrows). Thus the real valence band edge can be at more negative energy, but due to the higher tunneling barrier for the underlying cobalt electrons (because of the presence of the oxide island), tunneling through the oxide can be neglected for the STS measures.

3.4 Structural Model of CoO on Co bct

In this last section, the goal is to discuss how the cobalt oxide develops on the metastable body-centred-tetragonal (bct) cobalt structure. On the Fe(001)-p(1x1)O substrate the cobalt is known to grow, below about 15 ML, in the bct structure [70]. The in-plane lattice parameters are in register with the underlying iron (a=b=2.866 Å) while out-of-plane parameter is compressed (c=2.792 Å). The main reason for the above structure is that the bulk cobalt crystal has hcp (hexagonal close packed) structure which is more compact with respect to the bcc phase. Thus, while the cobalt remains in register with the iron, only the out of plane lattice parameter can change, thus increasing the mass density.

The cobalt oxide lattice parameter of rocksalt structure is a_{CoO}=4.267 Å, so the bct lattice parameter is too small to obtain regular defect free oxide islands. But, if we consider two bct unit cells (Fig.3.10 (a)), a compressed fcc (face centered cubic) lattice is obtained (dashed lines in the fig-

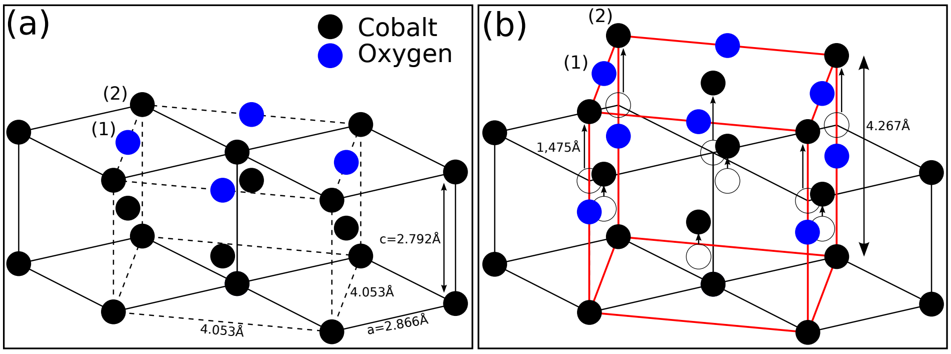

Figure 3.10: (a)-Two bcc lattice (straight line) which can be viewed as quasi-fcc (dashed line) lattice with the cubic parameters a=b>c. The oxygen is placed with respect to the p(1x1) symmetry. (b)-Model of the formation of the first layer of the oxide. The out of plane relaxation to the bulk value is assumed. The rocksalt lattice (without the lowest oxygen layer) is considered (red line). Empty circles represent the positions prior to the relaxation.

ure) with in-plane lattice parameter of $(a_{Fe}^2 \cdot 2)^{-1/2}=4.053$ Å and out-of-plane $c_{bct}=2.792$ Å. Thus the oxygen atoms of the Co(001)-*p*(1x1)O structure are already in the right positions for the rocksalt structure, which has a mismatch with the underlying cobalt of f=(4.267-4.053)/4.053=5.28%. As a result, the CoO [100] direction is parallel to the Fe [110] direction and also the respective [001] directions are parallel. The cobalt oxide thus, grows rotated in plane by 45° with respect to the cobalt in-plane bct structure.

The proposed model assumes that the out-of-plane lattice parameter is completely relaxed to the CoO bulk value (Fig.3.10 (b)). As a result, the oxide relative height with respect to the cobalt substrate is $a_{CoO}-c_{bct}=1.475$ Å. From the height analysis (Fig.3.7 (b)) we observed that, for high positive voltages, a plateau is reached at about 2 Å. This value is close to the calculated one if we also consider the biaxial strain (compression) which is expected to increase the of out-of-plane lattice parameter of CoO structure. As a conclusion, this simple model confirms that the CoO(001) phase has developed.

The evolution of the oxide has been studied up to a complete formation of the first CoO(001) layer. For total 15 L (Fig.3.11 (a)) the first layer is almost complete and the second layer islands are clearly visible (one island is circled in the figure). Exposing the sample to another 15 L of oxygen (total 30 L) the first layer is substantially complete and the evolution of the second one can be observed (Fig.3.11 (b)). In this latter figure, the larger islands are cobalt substrate islands.

On the 30 L exposed sample, the dual mode STM image was taken on

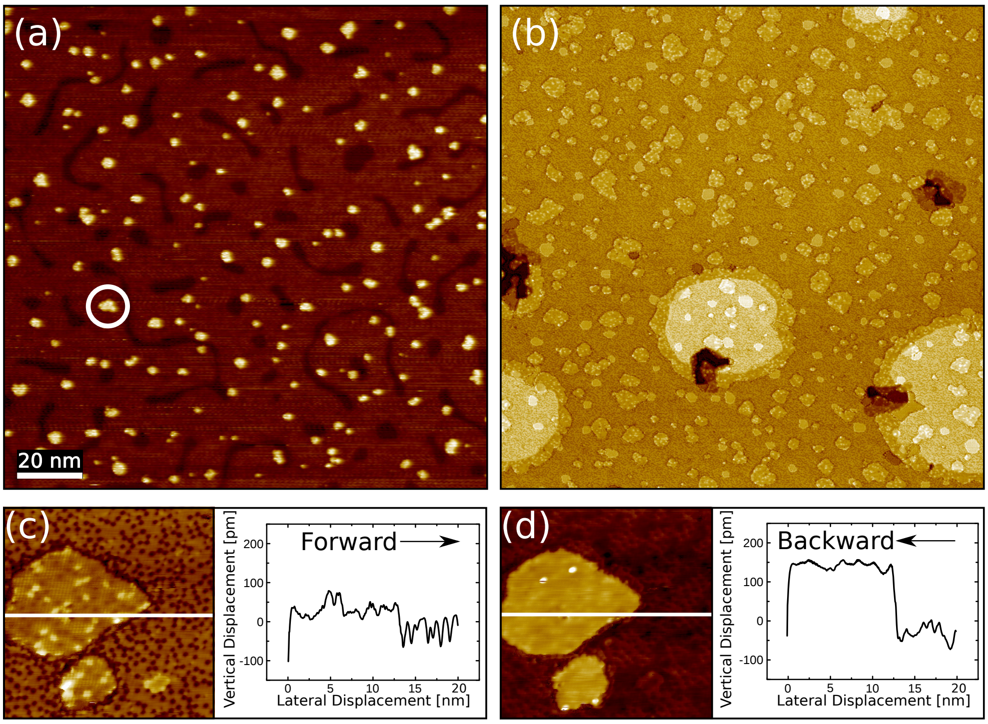

Figure 3.11: STM images (200x200 nm^2) of the cobalt exposed to total 15 L (a) and to 30 L (b) at 2·10^{-8}mbar. (a)-tunneling parameters: 1 V 200 pA. (b)-Tunneling parameters: 1 V 50 pA. (c) and (d)-Dual mode STM images on the oxide second layer with the respective vertical displacement profiles. (c)-tunneling parameters: 1 V 50 pA. (d)-tunneling parameters: -1.6 V 50 pA.

the second oxide layer. The tunneling current was kept fixed at 50 pA for both measures, while voltage is changed from 1 V to -1.6 V (Fig.3.11 (c) and (d) respectively). The height analysis of the second layer with respect to the cobalt substrate was not possible for the above image, while it was possible with respect to the first oxide layer. Unexpectedly, the behaviour of the relative height as a function of the applied voltage for the second layer is different with respect to the first layer. On the other hand, it was confirmed that these islands are oxide islands, because of the topographic inversion observed in STM at low voltages. The height analysis with respect to the substrate was possible in the sample where large cobalt islands were present[5].

The coverage, as a function of the exposure to oxygen (up to 120 L), were calculated for the first and the second oxide levels (Fig.3.12 (a)). The epitaxial layer-by-layer growth mode is confirmed from this measures.

---

[5] As earlier exposed, close to the step edges oxide develops faster.

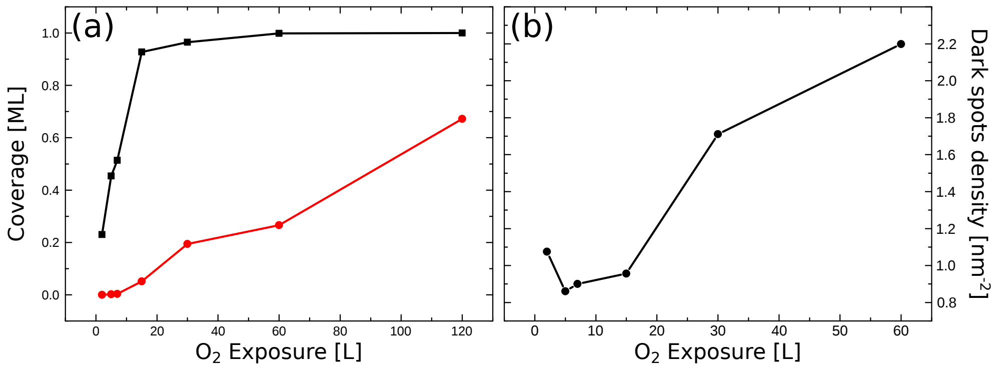

Figure 3.12: (a)-CoO coverage of the first and second layer (black and red curves, respectively) as a function of oxygen exposure. (b)-Dark spot density of the first oxide layer as a function of the oxygen exposure.

Also, the dark spot density, as a function of the exposure to oxygen (up to 60 L), was studied for the first oxide layer, while in the second layer dark spots were not detected. Only for voltages on which the STM images were acquired in the gap region, dark spots are visible. This suggests that these dark spots must be referred to the underlying cobalt oxide layer.

The dark spot density (Fig.3.12 (b)) increases by increasing the oxygen exposure in a way similar to the coverage trend, but a saturation was not observed. Considering the density at 60 L exposure we can infer that the dark spots tries to organize in $(\sqrt{5}\mathrm{x}\sqrt{5})\mathrm{R}\,27^\circ$ structure [71]. To explain this we can consider a $(\sqrt{5}\mathrm{x}\sqrt{5})\mathrm{R}\,27^\circ$ structure on top of a square lattice. The ratio between the density of the $(\sqrt{5}\mathrm{x}\sqrt{5})\mathrm{R}\,27^\circ$ structure and the density of the underlying lattice is 0.20. In fact, it can be seen that in this picture there is one atom of the $(\sqrt{5}\mathrm{x}\sqrt{5})\mathrm{R}\,27^\circ$ structure per 5 atoms of the (1x1) structure. In our case the density of the square lattice (i.e. of the Co(001)-p(1x1)O) is $(0.2866\,\mathrm{nm})^{-2}$=$12.17\,\mathrm{nm}^{-2}$, while the dark spots density, for 60 L exposure, is $2.2\,\mathrm{nm}^{-2}$. Dividing the latter density by the prior one we obtain 0.18, which is close to the theoretical value calculated before. For this reason we suppose that for higher exposures or heating the sample (in order to increase the diffusion in the surface of the dark spots) a perfect $(\sqrt{5}\mathrm{x}\sqrt{5})\mathrm{R}\,27^\circ$ structure might be obtained.

Conclusions

Early stages of oxidation of metastable bct cobalt were studied with the post-oxidation technique. Starting sample is Fe(001)-p(1x1)O. Successively 5 ML of Co were deposited using MBE. From AES data it was concluded that oxygen from the substrate floats to the Co surface and that there is negligible intermixing between iron and cobalt.

Heating the cobalt film at 200°C, a large flat surface is obtained. Exposing such a sample to the oxygen environment, a layer-by-layer growth mode of cobalt oxide is obtained. For 7 L exposure, oxide develops in circular-shaped islands that gradually coalesce up to 15 L, where a second oxide layer starts to grow. After 30 L of oxygen exposure, the first layer is almost complete and the second one is organized in separate islands.

A topographic study of the first oxide layer, for exposures at which the cobalt substrate is also visible, was performed using STM. A strong dependence of the relative height of the oxide with respect to the applied voltage and the tunneling current, was detected. Tunneling through the oxide layer has been observed when the tip Fermi level is aligned in the energy range within the electronic gap. In this situation, oxide islands are seen depressed with respect to the cobalt substrate. Conversely, for tunneling parameters for which tunnel in the conduction (or from the valence) band is possible, the oxide region has been observed as protruding islands.

From the STS data, a gap size of 2.3 eV was estimated and a shift of the Fermi level towards the conduction band was detected. As a consequence, charge transfer occurs, which produces band bending in the oxide.

Supported by the topographic study,a simple growth model of the cobalt oxide was proposed. In this picture CoO grows with the rocksalt structure rotated in plane by 45°, with respect to the bct cobalt lattice, exposing the (001) surface.

Bibliography

[1] P.A. Schweitzer. *Fundamentals of Metallic Corrosion: Atmospheric and Media Corrosion of Metals.* Taylor & Francis, Boca Raton, second edition, 2007.

[2] D.A. Jones. *Principles and Prevention of Corrosion.* Prentice Hall, Upper Saddle River, 1995.

[3] G. Ertl, H. Knözinger, F. Schueth, and J. Weitkamp. *Handbook of Heterogeneous Catalysis.* Wiley-VCH, Weinheim, second edition, 2008.

[4] A. Trovarelli. Catalytic properties of ceria and CeO_2-containing materials. *Catalysis Reviews*, 38(4):439–520, 1996.

[5] B. Yoon, H. Häkkinen, U. Landman, A. S. Wörz, J.-M. Antonietti, S. Abbet, K. Judai, and U. Heiz. Charging effects on bonding and catalyzed oxidation of CO on Au_8 clusters on MgO. *Science*, 307(5708):403–407, 2005.

[6] M. S. Chen and D. W. Goodman. The structure of catalytically active gold on titania. *Science*, 306(5694):252–255, 2004.

[7] K.J. Bachmann. *The Materials Science of Microelectronics.* VCH, New York, 1995.

[8] P. Torelli, E.A. Soares, G. Renaud, S. Valeri, X.X. Guo, and P. Luches. Nano-structuration of CoO film by misfit dislocations. *Surface Science*, 601(13):2651 – 2655, 2007.

[9] B. O'Regan and M. Grätzel. A low-cost, high-efficiency solar cell based on dye-sensitized colloidal TiO_2 films. *Nature*, 353:737–740, 1991.

[10] M. Imada, A. Fujimori, and Y. Tokura. Metal-insulator transitions. *Rev. Mod. Phys.*, 70:1039–1263, Oct 1998.

[11] Q. Wan, Q. H. Li, Y. J. Chen, T. H. Wang, X. L. He, J. P. Li, and C. L. Lin. Fabrication and ethanol sensing characteristics of ZnO nanowire gas sensors. *Applied Physics Letters*, 84(18):3654–3656, 2004.

[12] M. Finazzi, L. Duò, and F. Ciccacci. Magnetic properties of interfaces and multilayers based on thin antiferromagnetic oxide films. *Surface Science Reports*, 64(4):139 – 167, 2009.

[13] A. Hamnett and J.B. Goodenough. *Binary Transiton Metal Oxides.* Springer, Berlin, 1984.

[14] P.A. Cox. *Transition Metal Oxides.* Clarendon Pr, Oxford, 1992.

[15] J.W. Gibbs. *Reprinted in J.W. Gibbs: The Scientific Papers*, volume 1. Dover, New York, 1961.

[16] G. Kresse, S. Surnev, J. Schoiswohl, and F.P. Netzer. V_2O_3(0001) surface terminations: a density functional study. *Surface Science*, 555(1-3):118 – 134, 2004.

[17] C. T. Campbell. Ultrathin metal films and particles on oxide surfaces: structural, electronic and chemisorptive properties. *Surface Science Reports*, 27(1-3):1 – 111, 1997.

[18] S. Surnev, M.G. Ramsey, and F.P. Netzer. Vanadium oxide surface studies. *Progress in Surface Science*, 73(4-8):117 – 165, 2003.

[19] W. Weiss and W. Ranke. Surface chemistry and catalysis on well-defined epitaxial iron-oxide layers. *Progress in Surface Science*, 70(1-3):1 – 151, 2002.

[20] C. Noguera. *Physics and Chemistry at Oxide Surfaces.* University Press, Cambridge, 1996.

[21] A. Wander, I. J. Bush, and N. M. Harrison. Stability of rocksalt polar surfaces: An ab initio study of MgO(111) and NiO(111). *Phys. Rev. B*, 68:233405, Dec 2003.

[22] Hans-Joachim Freund. Introductory lecture: Oxide surfaces. *Faraday Discuss.*, 114:1–31, 1999.

[23] Gianfranco Pacchioni. Ab initio theory of point defects in oxide materials: structure, properties, chemical reactivity. *Solid State Sciences*, 2(2):161 – 179, 2000.

[24] G. H. Rosenblatt, M. W. Rowe, G. P. Williams, R. T. Williams, and Y. Chen. Luminescence of f and F^{+} centers in magnesium oxide. *Phys. Rev. B*, 39:10309–10318, May 1989.

[25] J. H. de Boer and E. J. W. Verwey. Semi-conductors with partially and with completely filled 3 d-lattice bands. *Proceedings of the Physical Society*, 49(4S):59, 1937.

[26] Z.-X. Shen, C. K. Shih, O. Jepsen, W. E. Spicer, I. Lindau, and J. W. Allen. Aspects of the correlation effects, antiferromagnetic order, and translational symmetry of the electronic structure of NiO and CoO. *Phys. Rev. Lett.*, 64:2442–2445, May 1990.

[27] N. F. Mott and R. Peierls. Discussion of the paper by de Boer and Verwey. *Proceedings of the Physical Society*, 49(4S):72, 1937.

[28] J. Zaanen and G.A. Sawatzky. Photoemission and the electronic-structure of transition-metal compounds. *Prog. Theor. Phys. Suppl.*, (101):231–270, 1990.

[29] E. Młyńczak, B. Matlak, A. Kozioł-Rachwał, J. Gurgul, N. Spiridis, and J. Korecki. Fe/CoO(001) and Fe/CoO(111) bilayers: Effect of crystal orientation on the exchange bias. *Phys. Rev. B*, 88:085442, Aug 2013.

[30] R. J. Powell and W. E. Spicer. Optical properties of NiO and CoO. *Phys. Rev. B*, 2:2182–2193, Sep 1970.

[31] J. van Elp, J. L. Wieland, H. Eskes, P. Kuiper, G. A. Sawatzky, F. M. F. de Groot, and T. S. Turner. Electronic structure of CoO, Li-doped CoO, and $LiCoO_2$. *Phys. Rev. B*, 44:6090–6103, Sep 1991.

[32] G. W. Pratt and Roland Coelho. Optical Absorption of CoO and MnO above and below the Néel Temperature. *Phys. Rev.*, 116:281–286, Oct 1959.

[33] I. Sebastian, T. Bertrams, K. Meinel, and H. Neddermeyer. Scanning tunnelling microscopy on the growth and structure of NiO(100) and CoO(100) thin films. *Faraday Discuss.*, 114:129–140, 1999.

[34] S. Sindhu, M. Heiler, K.-M. Schindler, W. Widdra, and H. Neddermeyer. Growth mechanism and angle-resolved photoemission spectra of cobalt oxide (CoO) thin films on Ag(100). *Surface Science*, 566-568, Part 1(0):471 – 475, 2004.

[35] K.-M. Schindler, J. Wang, A. Chassé, H. Neddermeyer, and W. Widdra. Low-energy electron diffraction structure determination of an ultrathin CoO film on Ag(001). *Surface Science*, 603(16):2658 – 2663, 2009.

[36] I. Sebastian and H. Neddermeyer. Scanning tunneling microscopy on the atomic and electronic structure of CoO thin films on Ag(100). *Surface Science*, 454-456(0):771 – 777, 2000.

[37] C. Giovanardi, L. Hammer, and K. Heinz. Ultrathin cobalt oxide films on Ir(100)-(1×1). *Phys. Rev. B*, 74:125429, Sep 2006.

[38] C. Ebensperger, M. Gubo, W. Meyer, L. Hammer, and K. Heinz. Substrate-induced structural modulation of a CoO(111) bilayer on Ir(100). *Phys. Rev. B*, 81:235405, Jun 2010.

[39] W. Meyer, K. Biedermann, M. Gubo, L. Hammer, and K. Heinz. Surface structure of polar Co_3O_4(111) films grown epitaxially on Ir(100)-(1x1). *Journal of Physics: Condensed Matter*, 20(26):265011, 2008.

[40] L. Gragnaniello, S. Agnoli, G. Parteder, A. Barolo, F. Bondino, F. Allegretti, S. Surnev, G. Granozzi, and F.P. Netzer. Cobalt oxide nanolayers on Pd(100): The thickness-dependent structural evolution. *Surface Science*, 604(21-22):2002 – 2011, 2010.

[41] M. De Santis, A. Buchsbaum, P. Varga, and M. Schmid. Growth of ultrathin cobalt oxide films on Pt(111). *Phys. Rev. B*, 84:125430, Sep 2011.

[42] S. I. Csiszar, M. W. Haverkort, Z. Hu, A. Tanaka, H. H. Hsieh, H.-J. Lin, C. T. Chen, T. Hibma, and L. H. Tjeng. Controlling orbital moment and spin orientation in CoO layers by strain. *Phys. Rev. Lett.*, 95:187205, Oct 2005.

[43] J.P. Velev, P.A. Dowben, E.Y. Tsymbal, S.J. Jenkins, and A.N. Caruso. Interface effects in spin-polarized metal/insulator layered structures. *Surface Science Reports*, 63(9):400 – 425, 2008.

[44] Hans Lüth. *Solid Surfaces, Interfaces and Thin Films.* Springer, fifth edition, 2010.

[45] Niklas Nilius. Properties of oxide thin films and their adsorption behavior studied by scanning tunneling microscopy and conductance spectroscopy. *Surface Science Reports*, 64(12):595 – 659, 2009.

[46] G. Binnig, H. Rohrer, Ch. Gerber, and E. Weibel. Surface studies by scanning tunneling microscopy. *Phys. Rev. Lett.*, 49:57–61, Jul 1982.

[47] J. Tersoff and D. R. Hamann. Theory of the scanning tunneling microscope. *Phys. Rev. B*, 31:805–813, Jan 1985.

[48] J.C.Chen. *Introduction to scanning tunneling microscopy.* Oxford University Press, New York, first edition, 1993.

[49] J.A. Stroscio and W.J. Kaiser. *Scanning Tunneling Microscopy.* Accademic Press, San Diego, first edition, 1993.

[50] Wiesendanger. *Scanning probe microscopy and spectroscopy.* University Press, Cambrige, first edition, 1994.

[51] D.J. Griffiths. *Introduction to Quantum Mechanics.* Pearson Prentice Hall, second edition, 2005.

[52] J. Bardeen. Tunnelling from a many-particle point of view. *Phys. Rev. Lett.*, 6:57–59, Jan 1961.

[53] R. J. Hamers. Atomic-resolution surface spectroscopy with the scanning tunneling microscope. *Annual Review of Physical Chemistry*, 40(1):531–559, 1989.

[54] R. Wiesendanger, H.-J. Güntherodt, G. Güntherodt, R. J. Gambino, and R. Ruf. Observation of vacuum tunneling of spin-polarized electrons with the scanning tunneling microscope. *Phys. Rev. Lett.*, 65:247–250, Jul 1990.

[55] K.H. Gundlach. Zur berechnung des tunnelstroms durch eine trapezförmige potentialstufe. *Solid-State Electronics*, 9(10):949 – 957, 1966.

[56] G. Binnig, H. Rohrer, Ch. Gerber, and E. Weibel. Tunneling through a controllable vacuum gap. *Applied Physics Letters*, 40(2):178–180, 1982.

[57] D. A. Bonnell. Scanning tunneling microscopy and spectroscopy of oxide surfaces. *Progress in Surface Science*, 57(3):187 – 252, 1998.

[58] U. Diebold. The surface science of titanium dioxide. *Surface Science Reports*, 48(5-8):53 – 229, 2003.

[59] Y. Wang, B. Meyer, X. Yin, M. Kunat, D. Langenberg, F. Traeger, A. Birkner, and Ch. Wöll. Hydrogen induced metallicity on the ZnO($10\bar{1}0$) surface. *Phys. Rev. Lett.*, 95:266104, Dec 2005.

[60] M. Sterrer, M. Heyde, M. Novicki, N. Nilius, T. Risse, H.-P. Rust, G. Pacchioni, and H.-J. Freund. Identification of color centers on MgO(001) thin films with scanning tunneling microscopy. *The Journal of Physical Chemistry B*, 110(1):46–49, 2006. PMID: 16471496.

[61] K. Højrup Hansen, T. Worren, E. Lægsgaard, F. Besenbacher, and I. Stensgaard. Bias dependent apparent height of an Al_2O_3 thin film on NiAl(110), and of supported pd clusters. *Surface Science*, 475(1-3):96 – 102, 2001.

[62] K. Meinel, A. Eichler, K.-M. Schindler, and H. Neddermeyer. STM, LEED, and DFT characterization of epitaxial ZrO_2 films on Pt(111). *Surface Science*, 562(1-3):204 – 218, 2004.

[63] H.-M. Benia, P. Myrach, and N. Nilius. Photon emission spectroscopy of thin MgO films with the STM: from a tip-mediated to an intrinsic emission characteristic. *New Journal of Physics*, 10(1):013010, 2008.

[64] S. Datta, W. Tian, S. Hong, R. Reifenberger, J. I. Henderson, and C. P. Kubiak. Current-voltage characteristics of self-assembled monolayers by scanning tunneling microscopy. *Phys. Rev. Lett.*, 79:2530–2533, Sep 1997.

[65] S. W. Wu, G. V. Nazin, X. Chen, X. H. Qiu, and W. Ho. Control of relative tunneling rates in single molecule bipolar electron transport. *Phys. Rev. Lett.*, 93:236802, Dec 2004.

[66] R. M. Feenstra. Tunneling spectroscopy of the (110) surface of direct-gap III-V semiconductors. *Phys. Rev. B*, 50:4561–4570, Aug 1994.

[67] G. J. de Raad, D. M. Bruls, P. M. Koenraad, and J. H. Wolter. Interplay between tip-induced band bending and voltage-dependent surface corrugation on GaAs(110) surfaces. *Phys. Rev. B*, 66:195306, Nov 2002.

[68] L. Jurczyszyn and B. Stankiewicz. Scanning tunneling spectroscopy of d states from a transition metal surface: theoretical study. *Vacuum*, 54(1-4):131 – 136, 1999.

[69] A. Picone, G. Fratesi, A. Brambilla, P. Sessi, F. Donati, S. Achilli, L. Maini, M. I. Trioni, C. S. Casari, M. Passoni, A. Li Bassi, M. Finazzi, L. Duò, and F. Ciccacci. Atomic corrugation in scanning tunneling microscopy images of the Fe(001)-$p(1 \times 1)$O surface. *Phys. Rev. B*, 81:115450, Mar 2010.

[70] S. K. Kim, C. Petersen, F. Jona, and P. M. Marcus. Ultrathin films of cobalt on Fe(001) and the effect of oxygen. *Phys. Rev. B*, 54:2184–2190, Jul 1996.

[71] A. Picone, G. Fratesi, M. Riva, G. Bussetti, A. Calloni, A. Brambilla, M. I. Trioni, L. Duò, F. Ciccacci, and M. Finazzi. Self-organized chromium oxide monolayers on Fe(001). *Phys. Rev. B*, 87:085403, Feb 2013.